https://doi.org/10.5194/egusphere-2026-6572
Preprint. Discussion started: 4 November 2026
© Author(s) 2026. CC BY 4.0 License.

Decadal transit times of flocculated mud in the Yukon River, Alaska are due to transient storage in river deposits

Joshua S. Anadu[1], Yutian Ke[1], Emily C. Geyman[1], Justin A. Nghiem[2], Jocelyn N. Reahl[3], Asiah L. Giuntoni[1], M. Isabel Smith[4], John S. Magyar[1], A. Joshua West[4], Woodward W. Fischer[1], and Michael P. Lamb[1]

[1]Division of Geological and Planetary Sciences, California Institute of Technology, Pasadena, CA 91125, USA
[2] Department of Earth Science, University of California, Santa Barbara, CA 93106, USA
[3] Department of Earth Science, University of Colorado, Boulder, CO 80309, USA
[4] Department of Earth Sciences, University of Southern California, Los Angeles, CA 90089, USA
Correspondence to: Joshua S. Anadu (janadu@caltech.edu)

Abstract. Mud particles comprise the vast majority of riverine sediment discharges and mediate the transfer of particulate organic carbon from terrestrial landscapes to deltas. Historically, mud particles were considered washload – sediment that may travel hundreds of kilometers without depositing, implying that rivers are fast paths through which mud-associated organic carbon exits terrestrial landscapes. However, recent studies have found that the interaction of particulate organic carbon and mud particles promotes flocculation, which enhances settling velocities, potentially driving mud and carbon deposition into the riverbed, point bars, and overbank deposits. Here, we study the transport of mud, developing and calibrating a statistical model based on particle hop lengths and transient storage residence times to investigate these processes for the Yukon River Basin, which has a carbon-rich, sub-arctic floodplain. From our field observations, we find that flocculated mud settles at about 2.86 mm s^{-1} and constitutes about 10% of the sediment in the active layer of the riverbed, 20% of the sediment in point bars, and 60% of the sediment in overbank deposits. Our model shows that 60–80% of mud particles transit the alluvial reaches of the Yukon River over decades, rather than the few weeks predicted if mud was a passive water tracer. Nearly all (~99.9%) of the decadal transit time is spent in the active layer of the riverbed, as opposed to the water column. 20–40% of mud particles enter floodplain storage during alluvial transit, extending their transit time from decades to centuries, or even millennia. Individual riverbed depositional events only last a few days because of rapid water column entrainment, whereas individual floodplain depositional events typically last centuries or longer, highlighting the dynamic nature of the riverbed. Consequently, transient storage in river deposits may allow substantial carbon dioxide and methane generation in rivers.

1 Introduction

The strong association between mud (particles of diameter < 63 μm) and particulate organic carbon in soils (Keiluweit et al., 2017; Churchman et al., 2020; Kleber et al., 2021; Georgiou et al., 2022) and sediments (Bock and Mayer, 2000; Curry et al., 2007; Faust et al., 2021) in rivers (Blair et al., 2004; Galy et al., 2008), lakes (Yu et al., 2009), and oceans (Blair and Aller, 2012; Middelburg, 2019) indicates that mud is the primary carrier of particulate organic carbon (POC) in Earth's

https://doi.org/10.5194/egusphere-2026-6572
Preprint. Discussion started: 4 November 2026
© Author(s) 2026. CC BY 4.0 License.

landscapes. The largest fluxes in the terrestrial POC cycle – the transfer of POC from soil-mantled hillslopes to river channels, riverine deposition of POC into floodplains, and river export of POC to nearshore sediments – are all driven by the redistribution of mud transiently stored in soils and sediments (Bianchi et al., 2024). Additionally, the physical and chemical association of OC with sediment has been shown to impact the reactivity of carbon (Hemingway et al., 2019; Repasch et al., 2021), thereby implicating mud as not only a carrier of organic carbon, but also as a modulator of its oxidation rate. Rivers have been recognized as central cogs in the global carbon cycle because they represent a fast path through which recently fixed biospheric organic carbon can be buried in ocean sediments, forming a geologic sink of atmospheric carbon dioxide (CO_2). However, in recent years, the paradigm surrounding fine sediment transport as a fast path has shifted based on the recognition that mud grains in rivers are transported as flocculated aggregates (Dunne et al., 2024; Fettweis et al., 2026; Schiller and Strom, 2026), settling at rates as much as 10^3 times faster than predicted by their individual grain diameters (Lamb et al., 2020a; Nghiem et al., 2022, 2024). Additionally, mounting evidence points to the fact that rivers are reactive environments, transforming much of the organic carbon delivered from terrestrial landscapes (Battin et al., 2023; Bianchi et al., 2024; Regnier et al., 2022).

To understand floc transport dynamics, efforts have been made to develop and evaluate physics-informed models that predict floc settling velocities (Strom and Keyvani, 2011; Lamb et al., 2020a; Nghiem et al., 2022, 2024), as well as the environmental, mineralogical, and organochemical controls on aggregate size in rivers (Zeichner et al., 2021; Nghiem et al., 2022). These models have found encouraging success (e.g., Osborn et al., 2023; Nghiem et al., 2025; Schiller and Strom, 2026), suggesting that mud interacts frequently with the riverbed and floodplain environments, and therefore potentially transits riverine corridors far slower than it would if it was a passive tracer of river water. If true, slower mud transit times could invalidate the view that mud-associated transport is a fast path through which organic carbon exits terrestrial landscapes and allows time for a greater amount of terrestrial organic carbon respiration and/or chemical transformation. Due to this uncertainty, the fraction of mud deposited into floodplains, rather than exported to continental margins, is one of the biggest uncertainties in the global mud–OC budget (Bianchi et al., 2024). In light of these recent findings, we ask: if mud is not following the river water as washload, then how long does it take to transit the alluvial reaches of rivers and where does it reside while in storage?

https://doi.org/10.5194/egusphere-2026-6572
Preprint. Discussion started: 4 November 2026
© Author(s) 2026. CC BY 4.0 License.

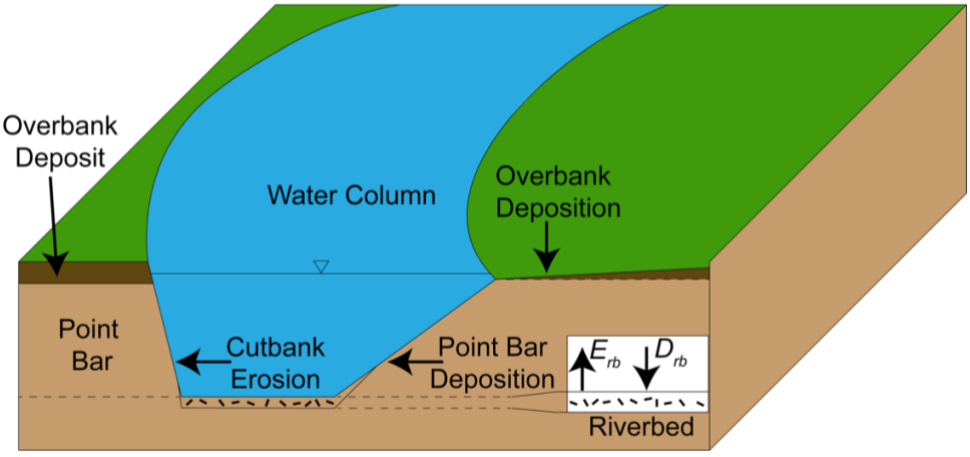


Figure 1: Schematic of the key mud reservoirs (the water column, active layer of the riverbed, point bars, and overbank deposits) and exchange fluxes (riverbed entrainment, riverbed deposition, cutbank erosion, point bar deposition, and overbank deposition) in a meandering alluvial river corridor. The water column transports mud downstream, constantly depositing mud onto the riverbed (D_{rb}) and entraining mud from the riverbed (E_{rb}). Lateral migration erodes mud from outer banks (point bars + overbank deposits) and deposits mud on inner banks (point bars). Lastly, overbank floods deposit mud on top of the floodplain.

A handful of approaches exist to determine alluvial sediment residence times. U-series chronometers are used to constrain the transit time of fine-grained sediments, based on the time since grains fell below the sand–silt grain size transition (DePaolo et al., 2006; Dosseto et al., 2008; Granet et al., 2010); however, recent studies observed large transit time uncertainties associated with small changes in key input parameters (Handley et al., 2013; Martin et al., 2019). Cosmogenic Beryllium-10 (^{10}Be) has been used to determine basin-averaged bulk sediment transit times (Repasch et al., 2020), but because rivers transport a spectrum of coarse to fine sediment particles, the underlying grain-size-specific transit time distribution is likely multimodal and skewed, complicating the interpretation of transit time distribution for mud particles. Herein we build on a third approach to use a statistical sediment budget to calculate the characteristic transport distance prior to sediment grain deposition (Lauer and Parker, 2008b; Bradley and Tucker, 2013; Pizzuto, 2014; Torres et al., 2017).

In a meandering alluvial river and its floodplain, there are four key reservoirs of mud: the river water column, the riverbed, point bar deposits built through river lateral migration, and overbank deposits accreted on the top of the floodplain during large floods. Together the point bar and overbank deposits make up the majority of the floodplain stratigraphy. In our current approach, we ignore secondary floodplain features such as abandoned channels, secondary channels, and crevasse splays. Mud exchange between the water column and the riverbed is primarily by riverbed entrainment and deposition, whereas mud exchange between the water column and the floodplain is governed by cutbank erosion, point bar deposition, and overbank deposition (Fig. 1). To build the statistical model for exchange probabilities between reservoirs, the characteristic distance a sediment grain is transported prior to deposition can be determined from a sediment mass balance framework. For example, Torres et al. (2017) defined a scaling parameter for the typical downstream distance particles are transported before being deposited in a point bar as,

https://doi.org/10.5194/egusphere-2026-6572
Preprint. Discussion started: 4 November 2026
© Author(s) 2026. CC BY 4.0 License.

$$L_{tran} = \frac{Q_s}{M_{avg} H_{pb}} \quad (1),$$

in which Q_s is the water column sediment discharge ($L^3\ T^{-1}$), M_{avg} is the river lateral migration rate ($L\ T^{-1}$) and H_{pb} is the point bar thickness (L). Equation (1) in a statistical model implies that the central tendency of the distribution of transport lengths can be determined from a calculation of the downstream distance required to exhaust the throughgoing sediment discharge. As highlighted by previous studies (Constantine et al., 2014; Geyman et al., 2025), Eq. (1) can be solved from time series measurements of river lateral migration and sediment discharge. However, grain size heterogeneity complicates this exercise. For example, mud dominates river sediment discharge but is believed to represent a minor fraction of point bar deposits, suggesting that transport lengths for mud particles are potentially much longer than would be determined from the bulk sediment approach presented in Eq. (1). Conversely, as compared to the bulk sediment-derived length scale, coarse sediment should experience shorter transport lengths before entering point bar deposits. Given that carbon is not uniformly apportioned across all grain sizes, it is not appropriate to take a bulk sediment approach to describe the transport behavior of sediment-associated organic carbon. Our goal is to develop a method that calculates the transit length scale with grain-size-specificity, so that we can quantitatively evaluate mud transit times. Additionally, while previous workers focused on water column–point bar exchange, we aim to extend the theory to include both water column–overbank and water column–riverbed exchange.

Here we investigate mud transit times in the Yukon River, a subarctic river possessing a vast, carbon-rich floodplain (Schuur et al., 2015; Lininger et al., 2019), potentially susceptible to accelerated degradation in response to temperature-amplified microbial decomposition (Schuur et al., 2022; Friedlingstein et al., 2026), as well as warming-driven hydrologic intensification (Beel et al., 2021), permafrost degradation (Chadburn et al., 2017), and bank erosion (Douglas et al., 2022; Geyman et al., 2024). To evaluate mud transit times, we need to determine if mud in the Yukon River is flocculated, as flocculation significantly increases mud depositional rates (Lamb et al., 2020a). Additionally, we need to constrain the mud fluxes from the water column to the riverbed, point bars, and overbank deposits, as these rates set the likelihood that a particle ends up in a given depositional reservoir. Finally, once mud deposits in any of the three reservoirs, we need to constrain typical particle residence times in each of these environments. Together this approach allows us to calculate mud transit times.

To answer these questions, we collected data pertaining to the river hydraulics, suspended sediment concentration, and suspended sediment granulometry (i.e., grain size statistics), to quantify mud discharges, as well as in situ mud settling velocities. From suspended sediment concentrations, granulometry, and mud settling velocities, we quantified the depositional flux of mud from the water column to the riverbed and overbank deposits. We introduced previously published lateral migration rates (Geyman and Lamb, 2026) and floodplain granulometric observations (Ke et al., 2026a) for our study area, to quantify the mud flux into point bars. From the mud fluxes, we derived process-specific mud transit length scales. With the suspended sediment data and bed sediment granulometry, we quantified the entrainment of mud from the riverbed into the water column, which we use to determine riverbed mud residence timescales. Lastly, we introduced previously developed floodplain storage theory to determine floodplain storage timescales (Geyman et al., 2025).

https://doi.org/10.5194/egusphere-2026-6572
Preprint. Discussion started: 4 November 2026
© Author(s) 2026. CC BY 4.0 License.

In the following section, we develop a statistical model that motivates our field measurements to constrain particle hop lengths, turnover time-derived riverbed storage timescales, and migration-derived floodplain storage timescales. In Section 3, we provide background on the Yukon River study area, field methods, and present additional field-specific sub-models that allow us to implement the statistical model presented in Section 2. In Section 4, we describe our field observations and implement the statistical transport model, presenting mud transit times for the Yukon River. In Section 5, we discuss the implications of our findings, focusing on the carbon cycle effects before concluding in Section 6.

2 Model Development

2.1 Model Concept and Goal

Our goal here is to quantify the transit time of mud in a generalized river system, and also to compute the proportion of time spent in the water column, riverbed, and floodplain. While each individual mud particle has a unique transit history, our approach is to develop a statistical model that allows for the characterization of the mud transit time distribution. For negatively buoyant suspended matter (i.e., sediment and particulate organic carbon), transport can be idealized into a series of discrete hops (Miller and Georgian, 1992; Cushing et al., 1993; Webster et al., 1999; Ganti et al., 2014; Pizzuto and Li, 2024; Schiller and Strom, 2026). During each hop, sediment is transported downstream for a characteristic distance before entering a transient deposit (i.e., riverbeds, point bars, or overbank deposits). Following the sediment budget approach (e.g., Eq. (1)) explored by previous workers (Lauer and Parker, 2008b; Pizzuto, 2014; Torres et al., 2017; Geyman et al., 2025), we relate the sediment fluxes from the water column into storage to the probability that a random particle enters storage. The characteristic downstream length scale (L_c; L) is the typical distance travelled by a particle before it deposits. Therefore, for the riverbed, point bars, and overbank deposits, the characteristic spatial frequency of depositional events (L_c^{-1}; L^{-1}) is the inverse of the characteristic transport length scale. The frequency at which sediment deposits into any of the three storage reservoirs is the sum of the process-specific depositional frequencies, $L_{c,tot}^{-1}$. Over a defined river reach (L), the transit time (T_t) is the cumulative time spent in either active transport (T_w) or storage (T_s),

$$T_t = T_w + T_s = \frac{L}{U} + \sum_{k=1}^{k=n} \tau_c \,, \qquad (2).$$

In Eq. (2), the cumulative active transport time is determined as the reach length divided by the depth-averaged flow velocity (U) and the cumulative storage time is the sum of the individual storage times. The total number of individual storage events, n, is approximated by $L/L_{c,tot}$. Additionally, the probability that a given depositional event, for example, occurs on the riverbed is the ratio of the process-specific depositional rate to the total depositional rate (e.g., $P_{rb} = L_{c,rb}^{-1}/L_{c,tot}^{-1}$). After deposition, sediment resides in each of these static reservoirs for a characteristic timescale (τ_c). It is then eroded and carried downstream in a subsequent transport hop. Thus, we turn to define appropriate relations that allow for the determination of grain size- and reservoir-specific characteristic transport length scales and storage timescales.

https://doi.org/10.5194/egusphere-2026-6572
Preprint. Discussion started: 4 November 2026
© Author(s) 2026. CC BY 4.0 License.

2.2 Characteristic Transport Length Scales

Equation (1) presents a turnover length scale, similar to the turnover time (Bolin and Rodhe, 1973), in which the throughgoing volumetric sediment discharge (L^3 T^{-1}) is divided by the per unit length flux of sediment deposited into point bars (L^2 T^{-1}), determining the downstream distance of lateral accretion required to exhaust the throughgoing water column reservoir. We sought to generalize this formulation, allowing for multiple depositional processes to occur simultaneously (Fig. 2). Analogous to the Exner equation (Paola and Voller, 2005), which equates changes in the mass of sediment in the water column to changes in the bed elevation, we begin by establishing a grain-size-specific water column mass (or equivalently volume) balance equation. Over a given river reach length (L), the instantaneous change in the volume of water column sediment with respect to time ($\partial V_{wc,i}/\partial t$) of grainsize class i is equal to

$$-\frac{1}{L}\frac{\partial V_{wc,i}}{\partial t} = \frac{\partial Q_{s,i}}{\partial x} + W_{bf}\left(D_{rb,i} - E_{rb,i}\right) - M_r\left[H_{pb,e}\left(f_{i,pb,e} - f_{i,pb,d}\right) + H_{ob,e}f_{i,ob,e}\right] + D_{ob,i}W_{ob}f_{i,ob} \quad (3).$$

in which the first term on the right-hand side is the divergence of the grain-size-specific sediment discharge ($\partial Q_{s,i}/\partial x$; L^2 T^{-1}), the second term represents the net flux of sediment between the riverbed and water column that are balanced when the grain-size-specific detrainment (or settling) flux ($D_{rb,i}$; L T^{-1}) is equal to the grain-size-specific entrainment flux ($E_{rb,i}$; L T^{-1}), but otherwise representing a net flux acting over the river width (W_{bf}; L). The third term describes the net release of sediment to the water column from lateral river migration. The migration rate (M_r; L T^{-1}) acts on both point bar and overbank deposits, which have thicknesses $H_{pb,e}$ and $H_{ob,e}$ (L), respectively. Importantly, we assume that thickness of eroding point bar deposits is the same as the depositing point bar ($H_{pb,e} = H_{pb,d} = H_{pb}$), neglecting subsidence and asserting a constant bankfull depth across kyr timescales (relevant for floodplain storage;). For a straight channel, migrating laterally with no curvature, the volume of sediment eroded from point bars is balanced by the volume of sediment deposited in accreting point bars, therefore, lateral migration would result in no net change in sediment stored in point bars. However, when considering specific grain size classes (e.g., mud), differences in the mud content between eroding and depositing point bars ($f_{m,pb,e} - f_{m,pb,d}$; dimensionless) would lead to non-zero mud fluxes between the water column and floodplain, as does the erosion of the grain-size-specific thickness of overbank material ($H_{ob}f_{i,ob,e}$). The final term $D_{ob,i}W_{ob}$, is the product of the grain-size-specific overbank detrainment flux ($D_{ob,i}$) and the inundated floodplain width during a flood (W_{ob}), neglecting floodplain entrainment. Lastly, for both riverbed and overbank reservoirs, the detrainment flux is the product of the near-bed grain-size-specific concentration and the particle settling velocity (e.g., $D_{rb,i} = C_{nb,i}w_i$), motivating the determination of in situ settling velocities, as well as representative grain-size-specific concentrations in both the near-bed regions of the channel ($C_{nb,i}$) and overbank ($C_{ob,i}$) flows.

https://doi.org/10.5194/egusphere-2026-6572
Preprint. Discussion started: 4 November 2026
© Author(s) 2026. CC BY 4.0 License.

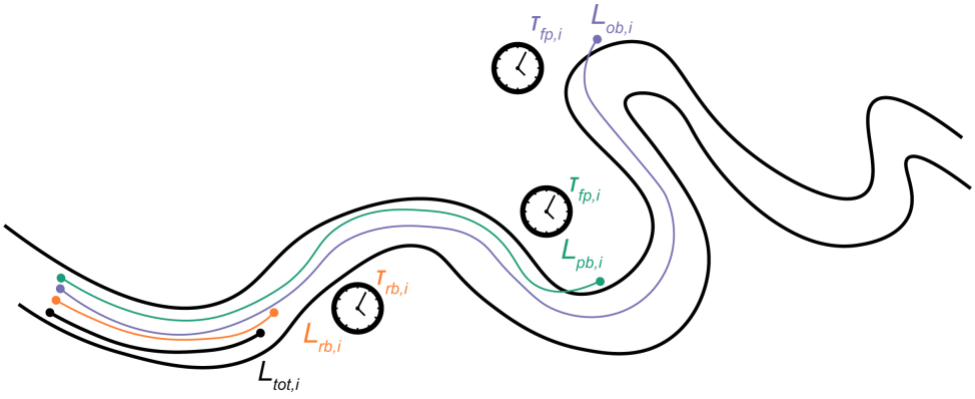


Figure 2: Conceptual diagram of the sediment transit model. For riverbed, point bar, and overbank deposition, their respective characteristic length scales (L_{rb}, L_{pb}, and L_{ob}) define the typical downstream transport distance before deposition. Combining the three depositional processes yields a characteristic transport length (L_{tot}) that is shorter than the process-specific length scales. The ratio of the process-specific transit length scales to the combined transit length scale can be used to calculate the probability of deposition into each reservoir. Once a sediment grain enters a deposit, sediment residence proceeds according to the process-specific characteristic residence timescale (τ_{rb} or τ_{fp}).

Equation (3) neglects the effects of channel curvature, which results in a greater volume of sediment eroded from ancient point bars than deposited in new point bars because the arc length of the outer bank is greater than the arc length of the inner bank. This geometric effect, termed channel extension by Lauer and Parker (2008b), results in the net transport of sediment from the floodplain to the water column. The magnitude of the effect of channel extension ($H_{pb}W_{bf}\kappa_{avg}f_{i,pb,e}$; where W_{bf} is the bankfull width and κ_{avg} is the average river curvature) is about 10% of the total volume of sediment eroded from point bars ($H_{pb}f_{i,pb,e}$). On long timescales, the net floodplain sediment loss from channel extension is balanced by oxbow lake filling. In any case, we choose to ignore this process because we confine the scope of our analysis to order of magnitude scaling. For this same reason, we neglect terms associated with the porosities of various deposits.

Next, we extend the concept presented in Eq. (1) to each of three depositional processes defined in Eq. (3) ($D_{rb,i}$, $D_{ob,i}$, and M_r). For each reservoir, we define the instantaneous transit length scale as the downstream length at which the grain-size-specific sediment discharge is equal to the product of the grain-size-specific detrainment flux and a characteristic width of deposition.

$$L_{rb,i} = \frac{Q_{s,i}}{r_{nb,i}\tilde{C}_i w_i W_{rb}\eta_{rb}} \tag{4a}$$

$$L_{ob,i} = \frac{Q_{s,i}}{r_{ob,i}\tilde{C}_i w_i W_{ob}\eta_{ob}} \tag{4b}$$

$$L_{pb,i} = \frac{Q_{s,i}}{M_r H_{pb} f_{i,pb,d}} \tag{4c}$$

Equation (4a) is the grain-size-specific riverbed analog of Eq. (1), whereby the throughgoing grain-size-specific sediment discharge is divided by the grain-size-specific settling flux from the near-bed region of the water column onto the riverbed. Similarly, Eq. (4b) performs the same calculation for an overbank flooding event. In Eq. (4a) and Eq. (4b), the terms η_{rb} and

https://doi.org/10.5194/egusphere-2026-6572
Preprint. Discussion started: 4 November 2026
© Author(s) 2026. CC BY 4.0 License.

η_{ob} (dim) are the trapping efficiencies for settling sediment grains, which we assume to be one for the present analysis (i.e., perfectly efficient trapping), allowing us to drop these terms from subsequent equations. Eq. (4c) is the grain-size-specific equivalent of Eq. (1), which in both cases only considers the settling flux into the small portion of the point bar balancing the bank erosion rate. As currently expressed, Eq. (4) defines the instantaneous characteristic length scales for deposition into the riverbed, point bar, and overbank, respectively. For convenience, Eq. (4) relates local concentrations to the depth-averaged concentration ($\tilde{C}$) through grain-size-specific reference concentration ratios, $r_{ob,i} = C_{ob,i}/\tilde{C}_i$ and $r_{nb,i} = C_{nb,i}/\tilde{C}_i$ (Parker et al., 1987). Therefore, Eq. (4) defines the instantaneous detrainment probabilities for each reservoir as a function of the downstream transport length, which when summed, defines the probability that a particle settles out of the water column.

Because both the sediment discharge and grain-size-specific settling fluxes vary throughout the hydrograph, instantaneous transit length scales in Eq. (4) may not appropriately capture long-term transport behavior. For example, if the discharge (Q_w) is below the bankfull discharge ($Q_{w,bf}$), the overbank detrainment rate is zero (i.e., a depositional hiatus), and therefore the overbank transit length scale is undefined. Rather than relying on instantaneous transit length scales, we derive characteristic transit length scales by integrating the instantaneous equations with respect to time over several years, weighting the instantaneous values calculated at each timestep by their contribution to the total sediment discharge over the timescale of integration (T). Therefore, the characteristic length scale (L_c), is the sediment-discharge weighted integral of the instantaneous transit length scales, which we evaluate for a given storage reservoir (i.e., rb, ob, and pb) and grain size class (i). Integrating Eq. (4) results in:

$$L_{c,rb,i} = \frac{1}{\int_0^T Q_{s,i} dt} \int_0^T Q_{s,i}\, \mathbf{1}_A(Q_w > 0) \frac{Q_{s,i}}{r_{nb,i}\tilde{C}_i w_i W_{rb}} dt \quad (5a)$$

$$L_{c,ob,i} = \frac{1}{\int_0^T Q_{s,i} dt} \int_0^T Q_{s,i}\, \mathbf{1}_A\left(Q_w > Q_{w,bf}\right) \frac{Q_{s,i}}{r_{ob,i}\tilde{C}_i w_i W_{ob}} dt \quad (5b)$$

$$L_{c,pb,i} = \frac{1}{\int_0^T Q_{s,i} dt} \int_0^T Q_{s,i}\, \mathbf{1}_A(M_r > 0) \frac{Q_{s,i}}{M_r H_{pb} f_{i,pb,d}} dt \quad (5c)$$

For the integration of the instantaneous length scales in Eq. (5) to be defined at all values of t, we introduce the indicator function ($\mathbf{1}_A$), which has a value of 0 when a process is inactive and 1 when a process is active. Riverbed deposition occurs when the discharge is greater than zero ($Q_w > 0$). Overbank deposition occurs when the discharge is greater than the bankfull discharge ($Q_w > Q_{w,bf}$). Point bar deposition occurs when the lateral migration rate is greater than zero ($M_r > 0$). Additionally, the instantaneous sediment discharges ($Q_{s,i}$) are weighted by the cumulative sediment discharge ($\int_0^T Q_{s,i}\, dt$). Importantly, the characteristic length scales determined according to Eq. (5) are predictive of long-term grain-size-specific detrainment rates. Having defined the appropriate characteristic length scales for each of the depositional processes, we turn to each of the characteristic transit length scale equations individually, providing useful simplifications and clarifications that aid in the practical application of each equation.

Beginning with the riverbed (Eq. (5a)), given that the sediment discharge is the product of the discharge and the depth-averaged sediment concentration, the latter term cancels with the same term in the denominator. Additionally, the

https://doi.org/10.5194/egusphere-2026-6572
Preprint. Discussion started: 4 November 2026
© Author(s) 2026. CC BY 4.0 License.

discharge is the product of the river width, depth, and average flow velocity, so the river width terms also cancel. Therefore, the integrand in Eq. (5a) simplifies to an advection length scale, $H_w U_w / w_i r_{nb,i}$, the characteristic horizontal distance traveled by a sediment particle before interacting with the riverbed (Fredsøe and Deigaard, 1992; Ganti et al., 2014; Lamb et al., 2010). Turning to the characteristic overbank transit length scale (Eq. (5b)), if we replace the total sediment discharge with the fraction of the sediment discharge conveyed by the floodplain ($Q_{s,ob,i}$), the equation simplifies to an overbank advection length scale, $H_{w,ob} U_{w,ob} / w_i r_{ob,i}$. Lastly, regarding the characteristic point bar transit length scale, if point bar heights ($H_{pb,e} = H_{pb,d} = H_{pb}$) and grain size compositions ($f_{i,pb,e} = f_{i,pb,d} = f_{i,pb}$) are constant, the integrand in Eq. (5c) simplifies to the ratio of the grain-size-specific sediment discharge and the migration rate, $Q_{s,i} / M_r$.

Overbank flow depths and flow velocities are shallower and slower than their channel counterparts, suggesting that overbank advection length scales are potentially shorter than riverbed advection length scales. However, during floods, the floodplain only conveys a fraction of the total sediment discharge ($Q_{s,ob,i} / Q_{s,i}$). Therefore, the distance required to exhaust the total sediment discharge by overbank settling is much longer than the overbank advection length scale, approximately by the factor ($Q_{s,i} / Q_{s,ob,i}$). Additionally, models of overbank deposition commonly assume that while sediment settles onto overbank deposits, the entrainment of sediment from floodplain surfaces can be neglected (Lauer and Parker, 2008a). Upon ignoring entrainment, the overbank settling flux decays exponentially from an initial value $C_{i,0}$ ($C_{i,0} = r_{ob,i} \tilde{C}_i w_i$; neglecting any differences between the depth-averaged and near-bed concentrations in the overbank water column) and approaches zero as the floodplain transport length (x_f) increases,

$$C_i = C_{i,0}\, exp\left(\frac{-w_i x_f}{H_{w,ob} U_{w,ob}}\right) \quad (6).$$

Notably, the length scale over which the sediment concentration decreases by a factor of $1/e$ is the advection length scale. Lauer and Parker (2008a) proposed a stream tube model of overbank deposition, wherein the integrated deposition rate along a stream tube is set by the initial sediment concentration ($C_{i,0}$), settling velocity (w_i), the per unit width discharge ($H_{w,ob} U_{w,ob}$), and the stream tube length (L_f),

$$D_{avg} = \frac{C_{i,0} H_{w,ob} U_{w,ob}}{L_f}\left[1 - exp\left(-\frac{w_i x_f}{H_{w,ob} U_{w,ob}}\right)\right] \quad (7).$$

Following Lauer and Parker (2008a), we propose that the stream tube length scales with the meander wavelength. Meander bends are typically 10 times the bankfull channel width (~10 km on the Yukon River). We approximate the typical stream tube length as half the meander bend wavelength, or 5 km (Text S1; Fig. S1a). Since floodplain channels are slower and significantly shallower than their mainstem counterparts, in addition to prior knowledge regarding typical in situ settling velocities for flocculated mud grains (Lamb et al., 2020a), our modeled floodplain stream tubes are much longer than the advection length scale. Therefore, for simplicity, we apply the limiting case ($L_f >> H_{w,ob} U_{w,ob} / w_i$), wherein $D_{avg} = C_{i,0} H_{w,ob} U_{w,ob} / L_f$. In Eq. (5b), we replace w_i with D_{avg}. Thus, our characteristic overbank transit length scale is only indirectly dependent on the grain-size-specific settling velocities, insofar as they control the near-surface sediment concentrations ($C_{i,0}$).

https://doi.org/10.5194/egusphere-2026-6572
Preprint. Discussion started: 4 November 2026
© Author(s) 2026. CC BY 4.0 License.

Our conceptual model treats the settling of individual grains into each of the three reservoirs as random, discrete, and independent (i.e., a Poisson process). Therefore, the characteristic length scales define scale factors for underlying exponential distributions. Lastly, while we have assumed perfectly efficient trapping, if, for example, 50% of mud grains that hit the bed were immediately re-entrained, then the entrainment rate of long-term riverbed material would decrease by 50%, proportionally increasing the residence time of mud that did enter long-term riverbed storage.

2.3 Characteristic Storage Time Scales

Now that we have derived the characteristic transit length scales for each of our three depositional reservoirs, we need the characteristic residence timescales experienced by particles deposited into each of these reservoirs. For the riverbed, we are interested in the stratum of sediment actively participating in downstream transport, assuming no long-term aggradation or degradation of the riverbed. Therefore, we confine our residence time calculation to the active layer (L_a), the topmost stratum of the riverbed involved in active sediment transport (Church and Haschenburger, 2017; Haschenburger, 1999). We determine the grain-size-specific thickness of the active layer by calculating the product of the cross-sectional area of the active layer ($W_{rb}L_a$; L^2) and the grain size fraction of the active layer ($f_{i,rb}$; dim). Subsequently, the instantaneous grain-size-specific residence time in the active layer is the grain-size-specific thickness of the active layer divided by the product of the river width and the grain-size-specific entrainment rate ($W_{rb}E_{rb,i}$; $L^2\ T^{-1}$),

$$\tau_{rb,i} = \frac{W_{rb}L_a f_{i,rb}}{W_{rb}E_{rb,i}} \quad (8a).$$

Fundamentally, Eq. (8a) calculates the riverbed mud turnover time – the time necessary for the entrainment flux to exhaust the mud reservoir in the active layer. As was the case for the instantaneous transit length scales (Eq. (4)), to capture the long-term riverbed residence time, we calculate a characteristic riverbed residence timescale. If mud behaves as equilibrium suspended bed material load, as previously observed (e.g., Lamb et al., 2020; Nghiem et al., 2025; Schiller and Strom, 2026), in Eq. (8) we can substitute $E_{rb,i}$ for $r_{nb,i}\tilde{C}_i w_i$.

Assuming the active layer depth and grain size fractions are constant in Eq. (8a), the characteristic riverbed residence timescale is set by the time-averaged mud entrainment rate,

$$\tau_{c,rb,i} = \frac{L_a f_{i,rb}}{T}\int_0^T \frac{1}{E_{rb,i}}\,dt \quad (8b).$$

From Eq. (8b), we can determine the long-term characteristic residence time of sediment deposited onto the riverbed, allowing us to account for transient riverbed storage in our transit time calculations. As for the assumption of a constant active layer depth, on short timescales, the active layer depth is set by the diameter of the uppermost grains that can be directly entrained by the flow (either into suspended or bedload). However, for rivers with bedforms (e.g., gravel sheets in multi-thread gravel-bedded rivers and dunes in sand-bedded rivers), bedform migration sets the depth-scale over which sediment is regularly transported in bedload and entrained into suspension (Rahuel et al., 1989; Wright and Parker, 2005; Brousse et al., 2018;

https://doi.org/10.5194/egusphere-2026-6572
Preprint. Discussion started: 4 November 2026
© Author(s) 2026. CC BY 4.0 License.

Vázquez-Tarrío et al., 2021). Bedforms are present in both the gravel- and sand-bed reaches of our field sites, so we consider the bedform depth the appropriate active layer depth for our analyses.

Previous workers have interrogated the controls on floodplain sediment residence timescales (Bradley and Tucker, 2013; Geyman et al., 2025; Limaye and Lamb, 2013; Torres et al., 2017), finding that the floodplain residence time is the time required for the river to rework previously deposited floodplain material. Geyman et al. (2025) determined that the floodplain age distribution, $g(t)$, is set by predictable river kinematic behavior and is best described by a broken power law, in which young deposits experience near complete preservation, after which deposit survivorship first decays according to a shallower power law slope, and later according to a steeper power law slope,

$$\frac{g(t)}{g(0)} = \left[1 + \left(\frac{\tau}{b_2}\right)^{1/s_2}\right]^{-1/m_2 s_2} \left[1 + \left(\frac{\tau}{b_3}\right)^{1/s_3}\right]^{-1/m_3 s_3} \quad (9).$$

In Eq. (9), $\tau = t/\tau_w$, τ_w = 300 yrs, b_2= 5.38, b_3= 211, m_2 = 0.636, m_3 = 7.92, s_2 = 0.613, and s_3 = 0.305. τ_w is the time required for the river to erode one channel width ($\tau_w = W_{bf}/M_{avg}$). b_3 is τ_{max}/τ_w, where τ_{max} is the time required to traverse the entire floodplain width ($\tau_{max} = W_{fp}/M_{avg}$; b_3 = 211 is appropriate for an unconfined floodplain). The floodplain storage time cumulative distribution function, F_t, is related to the floodplain age distribution,

$$F(t) = 1 - \frac{g(t)}{g(0)} \quad (10).$$

2.4. Total Transit and Storage Time

Putting it all together, for each simulation we initiate the particles in the water column, at a downstream distance of 0 km. We draw the time to the first depositional event from an exponential distribution, parametrized with the scale factor $L_{c,tot}^{-1}$. The depositional event is randomly assigned to a reservoir and the particle transit time and downstream distance are updated. Upon entering a storage reservoir, a particle resides in the respective reservoir for a timescale according to its residence time. For riverbed storage events, we draw the storage time from an exponential distribution, parametrized by the scale factor $\tau_{c,rb,i}$. As with mud settling from the water column, our model treats mud entrainment from the bed as a Poisson process, therefore described by an exponential distribution, in accordance with theoretical predictions for riverbed sediment residence time distributions on long timescales (Voepel et al., 2013). For floodplain deposition events, we draw the storage time (τ_{fp}) from the floodplain age distribution (Eq. (10)). In either case, we update the transit time, and the particle is transferred back to the water column. This process is repeated, updating the transit time and downstream distance until the downstream distance reaches the domain length.

Having developed a statistical framework that evaluates mud transport based on characteristic hop lengths and reservoir-specific storage residence times, we turn to introduce our field site, field methods, and auxiliary models required to apply the model developed in this section to the USGS historical gauge record at Stevens Village, AK.

https://doi.org/10.5194/egusphere-2026-6572
Preprint. Discussion started: 4 November 2026
© Author(s) 2026. CC BY 4.0 License.

3 Methods: Field Methods and Model Application

3.1 Yukon River Basin

The Yukon River Basin (YRB) is located in northwestern Canada and Central Alaska (AK) and has an area of 875,300 km^2, making it the fourth largest catchment in North America (Fig. 3; Brabets et al., 2000). The Yukon River begins at the Llewellyn Glacier in Canada, flows generally westward through Alaska, and empties into the Bering Sea. The rivers of the YRB are cryosphere-fed rivers, meaning that they predominantly source their discharge from snowmelt, glacial runoff, or lake runoff (sourced from snowmelt, ice melt, and rainfall). As with most cryosphere-fed rivers, discharge in the Yukon River is characterized by high seasonal variance (Brabets et al., 2000). Discharge peaks in the late spring as snowmelt triggers the freshet. Summer discharge is characterized by lesser contributions from snowmelt-dominated tributaries and increased contribution from glacial meltwater. Discharge in the late summer-early fall often also includes a significant contribution from rainfall. Winter (November–April) baseflow is significantly reduced compared to the ice-free season, reflecting low hydrologic connectivity in the frozen landscape.

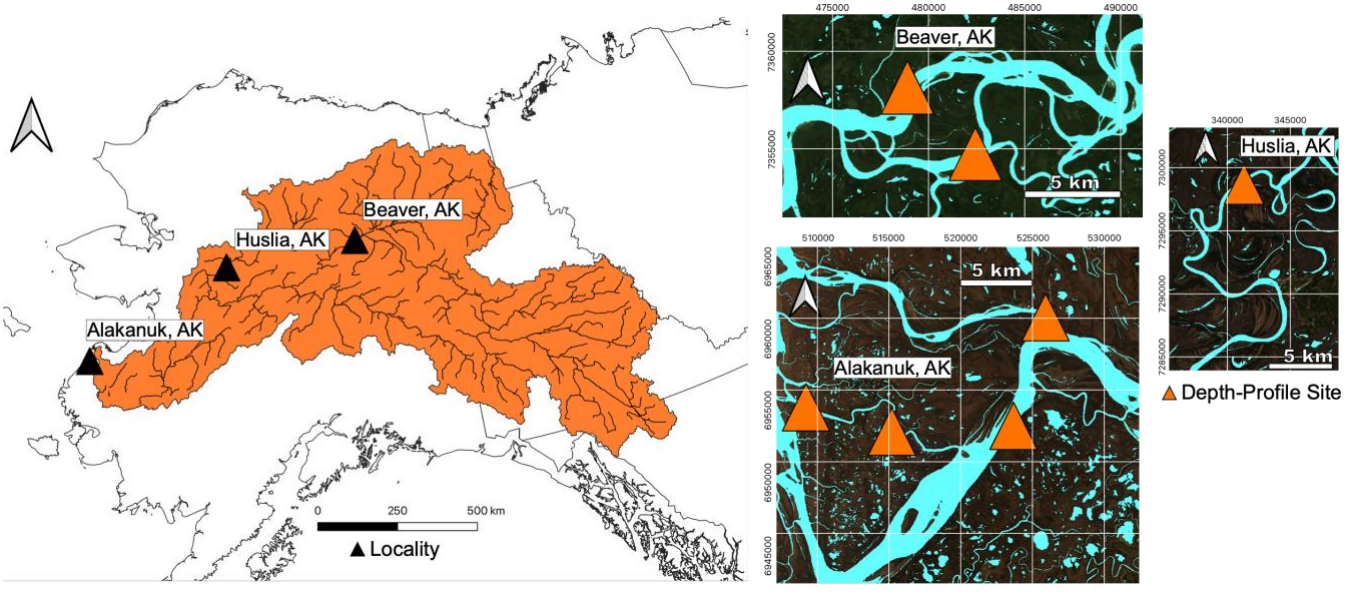


Figure 3: A basemap of the Yukon River Basin with the field localities marked (left). Beaver, AK (66.3576667°, -147.3983361°) is on the braided, gravel-bedded reach of the Yukon River, Huslia, AK (65.6992167°, -156.4021694°) is on the meandering, sand-bedded reach of the Koyukuk River, and Alakanuk, AK (62.6859556°, -164.6461389°) is on the sand-bedded distributaries of the Yukon–Kuskokwim Delta. Catchment outline and major rivers were obtained from HydroSHEDS (Lehner and Grill, 2013). Inset maps of the depth profile suspended sediment sampling sites (right). Binary water–land classification derived from Landsat-8 imagery. Landsat imagery courtesy of the US Geological Survey.

3.2 Field Campaign

Our characteristic transit length scale equation (Eq. (5)) describes sediment exchange dynamics between the water column and each of our three storage reservoirs along a timeseries. Therefore, central to our calculation is a timeseries of the

https://doi.org/10.5194/egusphere-2026-6572
Preprint. Discussion started: 4 November 2026
© Author(s) 2026. CC BY 4.0 License.

mud discharge, $Q_{s,m}$. A standard approach to calculating this timeseries relies on three pieces of information: 1) the discharge record, 2) a calibrated sediment rating curve, and 3) appropriate depth-averaged grain size fractions (i.e., $Q_{s,m} = Q_w \tilde{C} \tilde{f}_{m,wc}$). We turn to the USGS record for the discharge timeseries. The ArcticGRO monitoring campaign provides the paired discharge and suspended sediment concentration measurements necessary to build a rating curve (The Great Arctic Rivers Observatory, 2026). However, ArcticGRO suspended sediment samples were collected from surface waters and therefore underpredict depth-averaged sediment concentrations. A dataset of depth-resolved suspended sediment concentrations and grain size statistics can be used to calibrate the ArcticGRO record, improving the quality of the rating curve. Equations (5a) and (5b) also require mud settling velocities (w_m). Grain-size-specific concentration-depth profiles, the direct product of depth-resolved measurements of suspended sediment concentrations and granulometry, have been used extensively to calculate in situ mud settling velocities (e.g., Lamb et al., 2020; Lupker et al., 2011). Equation (8b) requires a representative bed mud content ($f_{m,rb}$), which can be determined from bed sediment surveys, and a timeseries of the mud entrainment rate ($E_{rb,m}$). By pairing suspended sediment surveys, bed sediment surveys, and river hydraulics surveys, previous workers have found that mud entrainment rates equal mud deposition rates (e.g., Lamb et al., 2020; Nghiem et al., 2025; Schiller and Strom, 2026), suggesting that mud settling rates ($r_{nb,m} \tilde{C}_m w_m$) can be used in place of mud entrainment rates. For these reasons, we collected depth-resolved suspended sediment samples ("depth profiles"), bed sediment samples, and conducted hydraulics surveys across the YRB.

Over the course of four consecutive field campaigns (spring 2022, fall 2022, spring 2023, and fall 2023), we collected suspended and bed sediment samples, in addition to hydraulics data from a boat. In the spring of 2022, sampling was conducted in the Koyukuk River near Huslia (about 280 km downstream of the USGS streamflow station at Hughes), as well as the two main branches of the Yukon River near Beaver (locally referred to as the Yukon and Wide rivers; about 180 km upstream of the USGS streamflow station at Stevens Village). We successfully completed both hydraulics surveys and suspended sediment sampling at all three depth profile sites. Bed sampling was also conducted at both locations, but suboptimal for the Yukon and Wide rivers, which we discuss in more detail in Section 3.3. In both locations, our sampling events closely corresponded with the freshet, the annual peak discharge associated with snowmelt. Notably, the Yukon River and Wide River sampling events near Beaver occurred at approximately bankfull conditions. Later that year in the fall, we returned to those three sites, collecting hydraulic, suspended sediment, and bed sediment data (unfortunately the bed sediment sample from the Yukon River near Beaver was lost). In the YRB, late summer hydrographs are characterized by secondary, pluvial-sourced peaks superimposed on the recession limb of the annual hydrograph following the freshet. In fall 2022, the rainfall surge nearly equaled the freshet discharge for the Koyukuk River and our sampling event occurred on the falling limb of this peak, whereas near Beaver, rainfall drove a relatively smaller surge in the Yukon River discharge.

In the spring of 2023, we returned to the sites near Huslia and Beaver but also conducted fieldwork at the Yukon–Kuskokwim Delta near Alakanuk (about 170 km downstream of the USGS streamflow station at Pilot Station). At all three localities, sampling events coincided with the freshet. In fact, sampling occurred during an overbank flooding event for the

https://doi.org/10.5194/egusphere-2026-6572
Preprint. Discussion started: 4 November 2026
© Author(s) 2026. CC BY 4.0 License.

Koyukuk River and approximately at bankfull discharge near Beaver and Alakanuk. On the Koyukuk River, hydraulic, suspended sediment, and bed sediment surveys were all conducted successfully. Near Beaver, hydraulic surveys were successfully conducted for both rivers but suspended and bed sediment sampling was only performed at the Yukon River site (due to complications associated with inclement weather). At the Yukon Delta, hydraulic surveys and suspended sediment sampling were successfully conducted at four sites (at high and low tide on the Yukon River, at two locations on the Alakanuk Pass, and on the Kwiguk Pass). Bed sediment sampling was also conducted at each of these locations. However, for both the high and low tide samples collected on the Yukon River, sampling was conducted using a Van Dorn sampler dragged along the riverbed, potentially biasing these samples. In the fall of 2023, we returned to the same sites. On the Koyukuk River, our sampling event occurred near baseflow. Near Beaver, sampling occurred on the recession limb of the summer rainfall surge, whereas at the delta, sampling coincided with the rainfall surge. Bed samples from the Yukon River near Beaver and the Kwiguk Pass were lost in transit. Lastly, we calculate seasonal riverbank erosion rates following Geyman and Lamb (2026), which we present as additional context for our suspended and bed sediment observations. Following the main field campaigns, in winter 2025, we collected both suspended sediment samples (Huslia, Beaver, and Alakanuk) and made hydraulics measurements (Huslia and Beaver) through holes augured in the river ice.

3.3 Hydraulics Measurements and Sediment Sampling

Depth profile sites were chosen in straight segments of the channels to minimize the hydraulic heterogeneity across the width of the river and sampling was always performed in the thalweg. At each depth profile site, we performed four acoustic Doppler current profiler (ADCP) transects (orthogonal to the current direction) to determine the hydraulic geometry (width, depth, velocity), as well as an additional survey in the thalweg to characterize the local velocity structure, and thus, the local bed shear stress. In conjunction, we collected suspended and bed sediment samples from a boat. For suspended sediments, we used either a 2 L, 4 L, or 8 L Van Dorn sampler depending on the sediment concentration. For bed sediments, we used a Ponar 'grab' sampler.

We follow the sampling procedure described by Ke et al. (2026), which we previously discussed in an accompanying data report (Anadu et al., 2025). In brief, sediment samples were collected from a boat drifting downstream above the target location. For suspended sediment, the Van Dorn was lowered to the appropriate depth by metering out rope and the sampler doors were triggered above the target location. The depths for suspended sediment sampling were chosen such that they adequately sample the power law concentration-depth profile predicted by Rouse theory. For bed sediment, the Ponar was lowered approximately 1 m above the riverbed and dropped onto the target location. In either case, the sampler was hauled back onto the boat, after which the sample was transferred into a small plastic bag using a funnel. A squeeze bottle was used to wash residual sediment into the bag. This process was repeated until samples at all target depths were collected. Sample bags were labeled and stored in a cooler. The sample retrievers wore nitrile gloves to minimize sample contamination. In the field, samples were filtered through a 0.22 μm polyethersulfone (PES) filter to recover sediment. Filters were frozen, transported back to the laboratory, and stored frozen until sediment retrieval. Lastly, throughout the field season, we used a

https://doi.org/10.5194/egusphere-2026-6572
Preprint. Discussion started: 4 November 2026
© Author(s) 2026. CC BY 4.0 License.

Real-Time Kinematic (RTK) GPS system to determine the water surface slope across the study reach, providing an estimate of the reach-averaged bed shear stress.

For the wintertime sampling efforts (2025), samples were collected at the depth profile sites after drilling through the river ice using an auger. We opportunistically collected suspended sediment samples in 150−1000 mL bottles, which were not lowered through the ice, but rather sampled waters ~10 cm below the surface of the hole in the ice. These are non-ideal sampling conditions, but we chose to include them given the paucity of data on sub-ice fluvial transport dynamics. Additionally, we conducted point ADCP surveys through the ice hole, collecting depth and velocity data in the thalweg of our previously surveyed channel cross sections. With the flow depth information, we were able to determine wintertime cross sectional area computationally by lowering the stage at the previously surveyed cross sections (Text S2; Fig. S2; Table S1). We then estimated discharge as the product of the cross-sectional area and the depth-averaged flow velocity from the point survey.

Our Ponar failed to accurately sample the bed sediment in gravel-bedded rivers. As a result, the bed grain size distributions in Beaver are significantly biased against large grain size clasts. During sampling, we generally recovered 0–5 clasts larger than the sand-sized fraction, insufficient for statistical characterization of the grain size distribution of the gravel fraction. However, we believe our sampling methodology has accurately sampled the less than 2 mm (sand–clay) fraction of the bed sediment. Later, we discuss how we augment the observed grain size distribution to approach a plausible grain size distribution for a gravel-bedded river. Lastly, both bed sediment samples (high and low tide) collected in the Yukon River near Alakanuk in spring 2023 were collected by dragging the Van Dorn on the riverbed because we had no available Ponar, potentially introducing sampling bias.

3.4 Sample Processing

In the lab, sediment was carefully scraped off the filter paper using tweezers, and residual sediment was retrieved via sonication in Milli-Q® water (resistivity of 18.2 MΩ·cm at 25 °C). Subsequently, the samples were centrifuged and the supernatant was decanted. Then, samples were freeze dried (or oven dried in the case of the winter samples) and weighed to determine the sediment concentration. Samples were homogenized and split using the cone and quarter method. Our grain size measurements require approximately 0.1 grams of sediment for robust determination of the distribution. Grain size splits were decarbonated with 1 M HCl (60°C; overnight). Following decarbonation, the acid was neutralized via repeated dilution. Organic matter was removed from the grain size splits with 30% hydrogen peroxide (60°C for 1 h, then overnight at room temperature). The following day, the hydrogen peroxide was removed via dilution. Sediment was dispersed in a 2 g/L sodium hexametaphosphate solution and sonicated for 10 minutes. Finally, the grain size distributions for each sample were measured using a Malvern Mastersizer 3000E laser diffraction particle size analyzer with a non-spherical scattering model. The volume-based grain size distributions from 0.2 to 2100 μm were reported as volume fractions in 100 logarithmically spaced bins (Anadu et al., 2025).

https://doi.org/10.5194/egusphere-2026-6572
Preprint. Discussion started: 4 November 2026
© Author(s) 2026. CC BY 4.0 License.

3.5 Grain-Size-Specific Concentration-Depth Profiles

To determine the mud settling rate, we adapt classical suspended sediment theory to predict near-bed grain-size-specific concentrations and settling velocities. Suspended sediment behavior is often described using Rouse theory (Rouse, 1937; Vanoni, 1946),

$$\frac{C}{C_a} = \left[\frac{\frac{H_w - z}{z}}{\frac{H_w - a}{a}}\right]^P \quad (11),$$

where C ($L^3\,L^{-3}$) is the volumetric sediment concentration at elevation (z; L) above the bed, C_a ($L^3\,L^{-3}$) is the near-bed concentration at reference elevation ($z = a$; L), and H_w (L) is the flow depth. P denotes the dimensionless Rouse number,

$$P = \frac{w_s}{\beta \kappa u_*} \quad (12),$$

where w_s ($L\,T^{-1}$) is the particle settling velocity, κ is the dimensionless von Karman constant of 0.41, u_* ($L\,T^{-1}$) is the bed shear velocity, and β is a dimensionless factor that accounts for differences between the turbulent diffusivity of sediment and the parabolic eddy viscosity model used to derive the Rouse equation (Graf and Cellino, 2002), which we assume to be unity for all suspended sediment (Nghiem et al., 2024). Using a grain-size-specific formulation of the Rouse–Vanoni equation,

$$\frac{C_i}{C_{a,i}} = \left[\frac{\frac{H_w - z}{z}}{\frac{H_w - a}{a}}\right]^{P_i} \quad (13),$$

we apply Rouse theory to individual grain size classes. With both the total concentration and grain size distribution for each suspended sediment sample in a depth profile, we construct grain-size-specific concentration-depth profiles by multiplying the total sediment concentration by the volume fraction of each grain size class at every depth. Following previous workers (Lamb et al., 2020a; Nghiem et al., 2022), we fit the log-linearized Rouse-Vanoni equation to grain-size-specific concentration-depth profiles using ordinary linear least-squares regression. From the fitting procedure, we recover the grain-size-specific Rouse number (P_i; the slope), as well as the grain-size-specific near-bed concentration ($C_{a,i} = r_{nb,i}\tilde{C}_i$; the intercept). Using shear velocity estimates from the depth-slope product, we calculate the grain-size-specific settling velocity as

$$w_i = P_i \beta \kappa u_* \quad (14).$$

We interpret the fitted settling velocity in Eq. (14) to represent the average behavior of sediment grains in each class, therefore, allowing us to characterize the grain-size-specific settling rates. Additionally, from the grain diameter-settling velocity ($D_i - w_i$) relationship determined for each depth profile, we identify the floc cutoff diameter (D_{ts}) by eye as the diameter at which the settling velocity begins to depart significantly from conventional settling velocity theory ($w_i = (R_s g D^2)/\left(c_1 \nu + \sqrt{0.75 c_2 R_s g D^3}\right)$; Ferguson and Church, 2004). In the settling velocity equation, R_s is the submerged specific gravity, g is the gravitational acceleration (m s^{-2}), D is the grain diameter (m), ν is the kinematic viscosity of water ($m^2\,s^{-1}$), and c_1 and c_2 are dimensionless constants.

Rouse theory casts the concentration of sediment in the water column as the equilibrium balance between the turbulence-driven entrainment (u_*) of sediment from the bed into the water column and the gravitational settling of sediment

https://doi.org/10.5194/egusphere-2026-6572
Preprint. Discussion started: 4 November 2026
© Author(s) 2026. CC BY 4.0 License.

(w_i). In conjunction with the bed material grain size fraction ($f_{b,i}$), empirical models (e.g., de Leeuw et al., 2020) have been developed to predict the near-bed concentration of sediment of a particular grain size ($C_{a,i}$),

$$C_{a,i} = A f_{b,i} (u_{*sk}/w_i)^a Fr^b \quad (15).$$

where u_{*sk} is the skin friction component of the shear velocity, Fr is the Froude number, and A (4.74 x 10^{-4}), a (1.77), and b (1.18) are all dimensionless constants.

For both sand (de Leeuw et al., 2020) and flocculated mud (Lamb et al., 2020a), Eq. (15) has been found to be generally predictive of suspended sediment concentrations. However, with regards to flocculated mud, Nghiem et al. (2025) observed disagreement between the observed and predicted floc concentrations in channels with high bed mud content. They hypothesized that this discrepancy could be because flocs are larger in the near-bed region than suggested by the analysis of a diameter-settling velocity ($D_i - w_i$) plot, obtained from Eq. (14). Larger near-bed flocs would increase floc settling velocities and decrease near-bed floc concentrations. This hypothesis is consistent with experimental floc observations, which found that floc-floc interactions on the riverbed tended to grow flocs, but these larger flocs rapidly returned to an equilibrium state when resuspended (Tran and Strom, 2019). Nghiem et al. (2025) proposed an entrainment floc cutoff diameter (D_{te}), which may differ from D_{ts}. Following their study, we define the entrainment cutoff diameter as

$$D_{te} = \gamma D_{ts} \quad (16),$$

where γ is the floc entrainment factor. The entrainment floc cutoff diameter is defined as the diameter for which the predicted near-bed floc concentration agrees with the measured floc concentration and the observed floc entrainment factor is the ratio of the entrainment floc cutoff diameter and the water column floc cutoff diameter. The authors proposed an empirical equation to predict the floc entrainment factor, which was calibrated on a river data compilation presented in Nghiem et al. (2022) and has not been tuned to fit the current dataset. The predicted floc entrainment factor is defined as

$$\gamma = 3.19 \left(f_{b,floc} \frac{D_{50}}{D_{ts}} \right)^{0.505} \quad (17),$$

where $f_{b,floc}$ is the fraction of bed material finer than the floc cutoff diameter and D_{50} is the median bed grain size diameter.

In summary, first we assess whether mud suspended sediment concentrations agree with theoretical predictions for individual mud grains by comparing the empirical predictions for disaggregated mud grains (Eq. (15)) against the near-bed concentration recovered from the linear regression (performed on the log-transform of Eq. (13)). Next, we perform the same entrainment analysis, assuming mud is flocculated and that the floc cutoff diameter can be inferred directly from the $D_i - w_i$ relationship for each profile. To perform the entrainment analysis on the flocculated mud class, we sum the concentrations of all grain size classes finer than the floc cutoff diameter at each depth in a depth profile and then refit the Rouse–Vanoni equation, recovering the measured near-bed floc concentration. To calculate the predicted near-bed floc concentrations, we sum the grain size fractions of all riverbed material finer than the floc cutoff diameter, update the settling velocity to reflect Stokes' settling at the floc cutoff diameter, and recalculate the predicted near-bed concentration following Eq. (15). Lastly, we perform the same analysis using the entrainment floc cutoff diameter, which we obtain following Eqs. (16)–(17) (Nghiem et al., 2025).

https://doi.org/10.5194/egusphere-2026-6572
Preprint. Discussion started: 4 November 2026
© Author(s) 2026. CC BY 4.0 License.

To perform the entrainment analysis, we need to accurately determine the volume fraction of each grain size class relative to the whole bed grain size distribution ($f_{b,i}$), which we do not have for the surveys conducted near Beaver at the depth-profile locations. To estimate this, we sieved bank samples (n=7), collected from exposed gravel bar deposits, at the 2 mm grain size. We recorded the mass fraction (or equivalently volume fraction as we assumed all clasts have the same density) of the total bank sample that was finer than 2 mm and found the mean value to be 0.226. Therefore, we estimate the true volume fraction of a grain size class by multiplying our observed grain size fraction by 0.226, our estimate of the total fraction of bed sediment finer than 2 mm. Our estimate agrees with a prior estimate of 0.2, derived from complete bed sediment sieving of exposed gravel bar heads in the Yukon Flats region (Clement, 1999). Additionally, we calculate u_{*sk} using the Manning–Strickler relation, which requires knowledge of the bed grain roughness (k_s), typically defined as $k_s = 3D_{84}$ (see de Leeuw et al., 2020 for more detail). Given we did not recover the coarse fraction of the bed sediment during our sampling events, in the spring of 2022, we performed Wolman pebble counts on five exposed gravel bars. In total, we measured 404 clasts and found the D_{50} to equal 1.5 cm and D_{84} to equal 3 cm (Text S3; Fig. S3). Again, our estimate agrees with historical measurements, which found typical D_{50} and D_{84} values in the Yukon Flats to be around 1 cm and 2 cm, respectively (Clement, 1999). Additionally, a D_{84}/D_{50} ratio of 2, observed by both (Clement, 1999) and our study, agrees with prior estimates from compiled data on gravel-bedded rivers (Rickenmann and Recking, 2011; Recking, 2013). Therefore, we proceed with using 3 cm as a representative D_{84} for both the Yukon and Wide rivers near Beaver. We filtered out low-quality data following de Leeuw et al. (2020) and rebinned our suspended sediment grain distributions from the reported 100 grain size bins to 50 grain size bins. In a preliminary analysis, we found using 50 grain size bins, we retain grain size specificity in our analyses and decrease analytical uncertainties caused by low mass fractions in finely spaced bins.

To calibrate the rating curve generated from the ArcticGRO surface sediment samples, we used our grain-size-specific concentration-depth profiles to calculate the depth-averaged sediment concentration ($\tilde{C}$) and grain size fractions ($\tilde{f}_i$). From our profiles, we have both the sediment concentration and grain size distribution at discrete depths. To account for unsampled regions of the water column, each profile was extended to the water surface and riverbed. For the shallow region, we extrapolated the observed concentration at the shallowest depth (typically 0.1 m below the surface) to the surface. For the near-bed region, we multiplied the observed concentration at the deepest depth by 1.66 and extrapolated it to the bed, following de Leeuw et al. (2020). To calculate a depth-averaged suspended sediment concentration, we numerically integrated the observed concentrations using the trapezoidal rule after log-transforming the sample depths. Similarly, to calculate the depth-averaged grain size distribution, we perform the same log-trapezoidal integration for each grain size class and then normalized all of the grain-size-specific concentrations by their sum. We find that the grain-size-specific numerical integration produced the same depth-averaged sediment concentration as the numerical integration performed on the entire sediment load (median percent difference of 0.65%), confirming the robustness of the calculation.

https://doi.org/10.5194/egusphere-2026-6572
Preprint. Discussion started: 4 November 2026
© Author(s) 2026. CC BY 4.0 License.

3.6. Model application to the Yukon

Our goal in Section 3 has been to develop the necessary scaffolding to apply the model developed in Section 2 to a timeseries dataset. In the preceding sections, we described our field surveys which provide point measurements of variables relevant for the characteristic transit length scales (Eq. (5)) and the characteristic riverbed residence timescale (Eq. (8b)). Here we describe our approach to develop timeseries of the model-relevant variables. Additionally, we describe our approach to integrate previously documented lateral migration rates (Geyman and Lamb, 2026) and floodplain granulometry (Ke et al., 2026a), relevant for the characteristic point bar length scale (Eq. 5c). We focus on mud transport, but the model can also be applied to sand.

3.6.1 River Hydraulics

From the discharge record, we need the hydraulic geometries of the discharge conveyed in the channel (H_w, W_w, and U_w) and the floodplain ($H_{w,ob}$, $W_{w,ob}$, and $U_{w,ob}$), which we achieve by calibrating a simplified, synthetic channel–floodplain complex to our field observations. We apply Manning's equation,

$$Q_w = \frac{1}{n} A R^{2/3} S^{1/2} \quad (18),$$

to a compound channel and floodplain to determine the relationship between river stage, total discharge, and hydraulic geometries of the channel and floodplain, respectively. In Manning's equation, n is the roughness coefficient, A is the cross-sectional area of the flow, R is the hydraulic radius (the area divided by the wetted perimeter), and S is the slope. We approximate the Yukon River as a single-thread, rectangular channel 1000 m wide and 7 m deep, appropriate bankfull values based on our field surveys. From our field surveys, we determined the bankfull discharge (14700 $m^3 s^{-1}$) and slope (2.47 x 10^{-4}), allowing us to calibrate the channel roughness (n = 0.027; s $m^{-1/3}$), a reasonable value for a natural channel (Arcement and Schneider, 1989). Given that our synthetic channel is rectangular, the channel width, W, does not vary as a function of discharge (i.e., $W = aQ_w^b$ where b = 0). Using field data collected by the USGS at Stevens Village, AK and Pilot Station, AK, we determined empirical b values of 0.07 and 0.09, respectively, approaching the rectangular channel endmember and supporting our assumption.

Next, we generate a simple floodplain elevation profile (hypsometry) with three simple rules. First, Ke et al., 2026b documented a relationship between the floodplain terrain age (t_{fp}) and the height above the bankfull datum (H_{ab}),

$$H_{ab} = 0.87 \log_{10}(t_{fp}) \quad (19).$$

This relationship encodes both the effects of overbank accretion and displacive ground-ice ingrowth. We set the cutbank to be the height of a 5000-year-old deposit (~3.22 m above the bankfull stage). Second, Geyman et al. (2025) found that decadal migration rates (~2.8 m yr^{-1} for the Yukon River) can explain the centennial–millennial river migration history recorded in the scroll bar sequences of the floodplain, suggesting that decadal bank erosion observations sufficiently encapsulate long-term variability and intermittency. On short timescales ($t \leq 3\tau_w$), we can combine these two rules on the point bar side of the floodplain, as the distance (x) from the inner bank increases,

https://doi.org/10.5194/egusphere-2026-6572
Preprint. Discussion started: 4 November 2026
© Author(s) 2026. CC BY 4.0 License.

$$H_{ab} = 0.87 \log_{10}(x/2.8), x \leq 3000 \quad (20a),$$

an approach that is quite similar to that of Lauer and Parker (2008a). In other words, the floodplain elevation linearly rises from the bankfull stage for the first 3 km from the inner bank (reaching a height of 2.6 m above the bankfull stage). After this distance, meander kinetics are characterized by random-walk-like behavior (Bradley and Tucker, 2013; Geyman et al., 2025), wherein $x \propto \sqrt{t}$. Therefore, beyond 3 km, the floodplain elevation rises more rapidly,

$$H_{ab} = 0.87 \log_{10}\left[\frac{3000}{2.8}(x/3000)^2\right], 3000 < x < 6497 \quad (20b),$$

until the inner bank elevation equals the cutbank elevation, approximately 6.5 km from the inner bank edge. After reaching the outer bank elevation, we do not further increase the inner bank elevation. In the model domain, both sides of the floodplain extend about 16 km from the edge of the channel (Text S1; Fig. S1b). We set the floodplain roughness (n = 0.054) to be twice the channel roughness, reasonable for a sparsely-vegetated floodplain (Arcement and Schneider, 1989).

After building the composite channel, we incrementally increased the water stage, calculating the hydraulic parameters for the channel and each side of the floodplain independently, assuming the floodplain conveys water at the same slope as the channel. Summing the individual discharges, we recover a stage-cumulative discharge relation. Therefore, with our calibrated composite channel, from historical discharge data, we can estimate the hydraulic properties of both the in-channel and floodplain conveyed discharges. To estimate the characteristic overbank length scale, when the stage is above bankfull, we combine the average floodplain water depth and velocity determined from the synthetic cross-section with the stream tube length as a simplified floodplain conveyance model intended to capture reach-averaged overbank deposition rates.

3.6.2 Sediment Rating Curve

To develop the sediment rating curve used to constrain depth-averaged sediment concentration in time (needed for Eq. (5)), we used

$$C = aQ^b \quad (21).$$

To constrain a and b, we used samples taken since 2003 at Pilot Station, AK, about 100 km upstream of the apex of the Yukon Delta (The Great Arctic Rivers Observatory, 2026). Surface suspended sediment concentrations ranged from 2.9 mg L^{-1} to 863 mg L^{-1}, while accompanying discharge measurements ranged from 1175 m^3 s^{-1} to 33414 m^3 s^{-1}. To convert surface concentrations into depth averaged concentrations, we can define a correction factor, $1/r$, which equates the surface sediment concentration to the depth-averaged sediment concentration (Text S4; Fig. S4). To incorporate grain-size-specificity, we use our depth profile surveys to determine the depth-averaged water column mud content ($\tilde{f}_m$), as well as the values of the mud reference concentration ratios, $r_{nb,m}$ and $r_{ob,m}$.

3.6.3 Lateral Migration

Equation (5c) also requires a time series of bank migration rates. We employ the entrainment- and thaw-limited erosion model from Geyman and Lamb (2026), which has been calibrated for the Yukon River. For entrainment-limited erosion,

https://doi.org/10.5194/egusphere-2026-6572
Preprint. Discussion started: 4 November 2026
© Author(s) 2026. CC BY 4.0 License.

$$E_{ent} = \frac{B}{\rho_b f_{sed}}\left(\frac{\rho_w C_f U^2}{(1+\epsilon)\tau_{crit}} - 1\right)^n \quad (22),$$

where B is an optimized erodibility coefficient (7.5 x 10^{-5} kg m^2 s^{-1}), ρ_b is the sediment bulk density (861 kg m^{-3}), f_{sed} is the sediment mass fraction in bank sediment (calculated as $f_{sed} = 1 - f_{ice}$, where f_{ice} is 0.236), ρ_w is the density of water (1000 kg m^{-3}), C_f is the friction coefficient (5 x 10^{-3}), U is the cross-sectionally averaged flow velocity, τ_{crit} is the bed shear stress (4.0 Pa), and n equals 1. The term $1/(1+\epsilon)$ approximates the bank shear stress from the bed shear stress, where ϵ is 0.2. A time series of the average channel flow velocity is determined as $U = Q_w/A_w$, where Q_w and A_w are the channel discharge and cross-sectional area, respectively. For thaw-limited erosion,

$$E_{thaw} = \frac{APr^{\alpha}Re^{\beta}\kappa_w(T_w - T_f)}{H_w\rho_b\left(L_f + c_p(T_f - T_i)\right)} \quad (23),$$

where A (1.78 x 10^{-6}), α (0.333), and β (0.927) are dimensionless empirical coefficients, Pr is the dimensionless Prandtl number (10), κ_w is the thermal conductivity of water (0.6 W m^{-1} °C^{-1}), T_w is the water temperature (°C), T_f is the fusion temperature of water (0°C), T_i is the initial bank temperature (-1°C), H_w is the flow depth, L_f is the permafrost latent heat of fusion (calculated as $L_f = f_{ice}L_{ice}$, where L_{ice} = 3.34 x 10^5 J kg^{-1}), and c_p is the permafrost heat capacity (J kg^{-1} °C^{-1}). The predicted erosion rate is the minimum of the thaw- and entrainment-limited erosion rates,

$$E = \text{argmin}(E_{ent}, E_{thaw}) \quad (24).$$

Geyman and Lamb (2026) attributed 1.46 m of the annual 2.8 m of erosion to ice break-up.

$$E_{tot} = E_{ice} + E \quad (25).$$

Therefore, the remaining 1.34 m of annual erosion should be attributed to thaw- and entrainment-limited fluvial erosion.

Applying the combined bank erosion model (Eqs. (22)–(24)) on our synthetic cross section over the historical gage record, the average annual riverine bank erosion rate is 1.78 m yr^{-1}. We apply a singular linear scaling to both A and B, such that the temporal trends in both erosion rates are maintained, but the average cumulative erosion from non-ice-induced erosion is 1.34 m. For the primary modeling effort, we initially ignore the erosion contribution from ice break-up. Subsequently, we present two end-member scenarios to constrain the effects of ice break-up. In the first scenario, a thermal break-up occurs every year, which we model by spreading the 1.46 m of ice-induced erosion over a three-week period. In the second scenario, a mechanical break-up occurs every year, which we approximate by inducing 1.46 m of bank erosion in 5 days. According to the Cold Regions Research and Engineering Laboratory (CRREL) Ice Jam Database, there have been 348 documented mechanical break-up events along the Yukon River since 1936 (White, 1996; U.S. Army Corps of Engineers, 2026). At any given location, these events typically happen every few years to about a decade, suggesting that true break-up behavior is an intermediate case between our end member scenarios. Finally, we are using the temporal pacing of bank erosion rates as a proxy for the pacing of point bar growth rates. The temporal dynamics between bank erosion and bar growth (i.e., bar-push vs. bank-pull) are not clear and remain a topic of debate (e.g., Eke et al., 2014; Parker et al., 2011; Mason and Mohrig, 2018, 2019; Martin et al., 2024), however, by equating the two rates, we are applying a constant width assumption.

https://doi.org/10.5194/egusphere-2026-6572
Preprint. Discussion started: 4 November 2026
© Author(s) 2026. CC BY 4.0 License.

3.6.4 Model Implementation

To implement our model, we generate time series of the hydraulic parameters (Eqs. (18)–(20)), sediment flux (Eq. (21)), and the bank erosion rates (Eqs. (22)–(25)). From these time series, we generate time series of the riverbed settling flux, the overbank settling flux, and the point bar growth flux. Next, we calculate the instantaneous transit length scales (Eq. (4)) and riverbed residence timescale (Eq. (8a)) along the time series. The characteristic transit length scales (Eq. (5)) and riverbed residence timescale (Eq. (8b)) are derived from the time series of instantaneous values. From the characteristic transit length scales, we obtain reservoir-specific interaction rates by multiplying the inverse of the characteristic length scales (L_c^{-1} values) by the water column mud transport velocity.

We assume the mud transport velocity in the water column is equal to the fluid velocity (McLean, 1992; Mehta and McAnally, 2013) and set this to a characteristic scale of 1 m s^{-1}, consistent with our ADCP measurements. We set the active layer depth to be 1 m, an appropriate value for both the migration of large gravel-sheet bodies (Brousse et al., 2018) and the migration of dunes in a 7 m deep, sand-bedded river ($H_d = H_w/7.7$, where H_d is the height of channel dunes and H_w is the river depth; Bradley and Venditti, 2017). Constrained by our field surveys (Sections 4.2–4.5), we use a constant near-bed mud reference concentration ratio ($r_{nb,m}$ = 1.41), overbank reference concentration ratio ($r_{ob,m}$ = 0.67), mud settling velocity (w_m = 2.86 mm s^{-1}), riverbed mud fraction ($f_{m,rb}$ = 0.103 by volume), water column mud fraction ($\tilde{f}_{m,wc}$ = 0.79), and point bar mud fraction ($f_{pb,m}$ = 0.211). Additionally, we set the mud entrainment rate equal to the mud settling rate, which we support with evidence in Section 4.4. Lastly, we highlight the effects of flocculation by presenting an unflocculated mud case, in which we set the mud settling velocity equal to 0.32 mm s^{-1} (Stokes' settling velocity for a 20 μm silt grain, approximately the median grain size across the YRB).

Particle transport and storage is calculated from Circle, AK, to the Yukon Delta (~1750 km). We chose Circle, AK, as the start of the model domain because upstream of Circle, AK, the Yukon River flows through a relatively narrow canyon with no significant floodplain. Downstream of Circle, AK, the Yukon is characterized by a laterally extensive floodplain except for the reach from Stevens Village, AK to Tanana, AK (approximately 225 km). For simplicity, our model permits riverbed and floodplain deposition along the entire reach from Circle, AK, to the Yukon Delta, likely overestimating the likelihood of floodplain storage.

We ran four sets of simulations. In the first set of simulations, we only allowed particle deposition onto the riverbed (i.e., bank erosion and overbank deposition are ignored). In the latter three sets of simulations, we allowed particle deposition in the riverbed and floodplain (point bar and overbank) storage reservoirs. In simulation two, floodplain erosion is based solely by the thaw- and entrainment-limited erosion model, whereas in the final two sets of simulations, we capture the observed annual erosion rate by including a contribution from ice-mediated erosion (one mechanical and one thermal breakup scenario). In all cases, we performed 10^7 simulations to estimate the transit time distribution.

https://doi.org/10.5194/egusphere-2026-6572
Preprint. Discussion started: 4 November 2026
© Author(s) 2026. CC BY 4.0 License.

4. Results

Before giving model results, we first describe our field observations emphasizing findings pertaining to depth-averaged grain size distributions, grain-size-specific settling velocities, grain-size-specific reference concentration ratios, and riverbed grain size compositions, which we integrate with floodplain grain size compositions reported by Ke et al. (2026a). In addition, tantamount to the application of our model is evidence that mud is not behaving like washload, but rather is interchanging between the water column, riverbed, and floodplain. Thus, we interrogate our field data for evidence of this behavior.

4.1 Field Observations Overview

In 2022, during the freshet, discharge at Huslia peaked at about 2000 $m^3 s^{-1}$ (Fig. 4a) and 14000 $m^3 s^{-1}$ near Beaver (Fig. 4b). Freshet bank erosion rates peaked at about 6 m yr^{-1} near Huslia (Fig. 4d) and 10 m yr^{-1} near Beaver (Fig. 4e). In the fall, discharge again peaked at about 2000 $m^3 s^{-1}$ at Huslia (Fig. 4a) but only reached values of about 7000 $m^3 s^{-1}$ at Beaver (Fig. 4b). Fall bank erosion rates near Huslia equalled the springtime (~6 m yr^{-1}; Fig. 4d), whereas erosion rates were about 5 m yr^{-1} near Beaver (Fig. 4e). In spring 2023, the freshet discharge peaked at about 4000 $m^3 s^{-1}$ at Huslia (Fig. 4a), 20000 $m^3 s^{-1}$ at Beaver (Fig. 4b), and 33000 $m^3 s^{-1}$ at Alakanuk (Fig. 4c). Bank erosion rates peaked at about 8 m yr^{-1} at Huslia (Fig. 4d), 8 m yr^{-1} at Beaver (Fig. 4e), and 16 m yr^{-1} at Alakanuk (Fig. 4f). The springtime erosion rates are much higher near Alakanuk than Beaver because erosion is not thaw-limited in the lower Yukon. Lastly, in the fall, discharge at Huslia rivalled the freshet (3500 $m^3 s^{-1}$; Fig. 4a), whereas at Beaver (7000 $m^3 s^{-1}$; Fig. 4b) and Alakanuk (15000 $m^3 s^{-1}$; Fig. 4c), the fall discharge was significantly lower than the spring. Near Huslia, fall bank erosion rates (~10 m yr^{-1}; Fig. 4d) exceeded spring bank erosion rates, a consequence of warmer summer waters. Near Beaver and Alakanuk, fall bank erosion rates peaked at about 5 m yr^{-1} (Fig. 4e) and 3 m yr^{-1} (Fig. 4f), respectively.

https://doi.org/10.5194/egusphere-2026-6572
Preprint. Discussion started: 4 November 2026
© Author(s) 2026. CC BY 4.0 License.

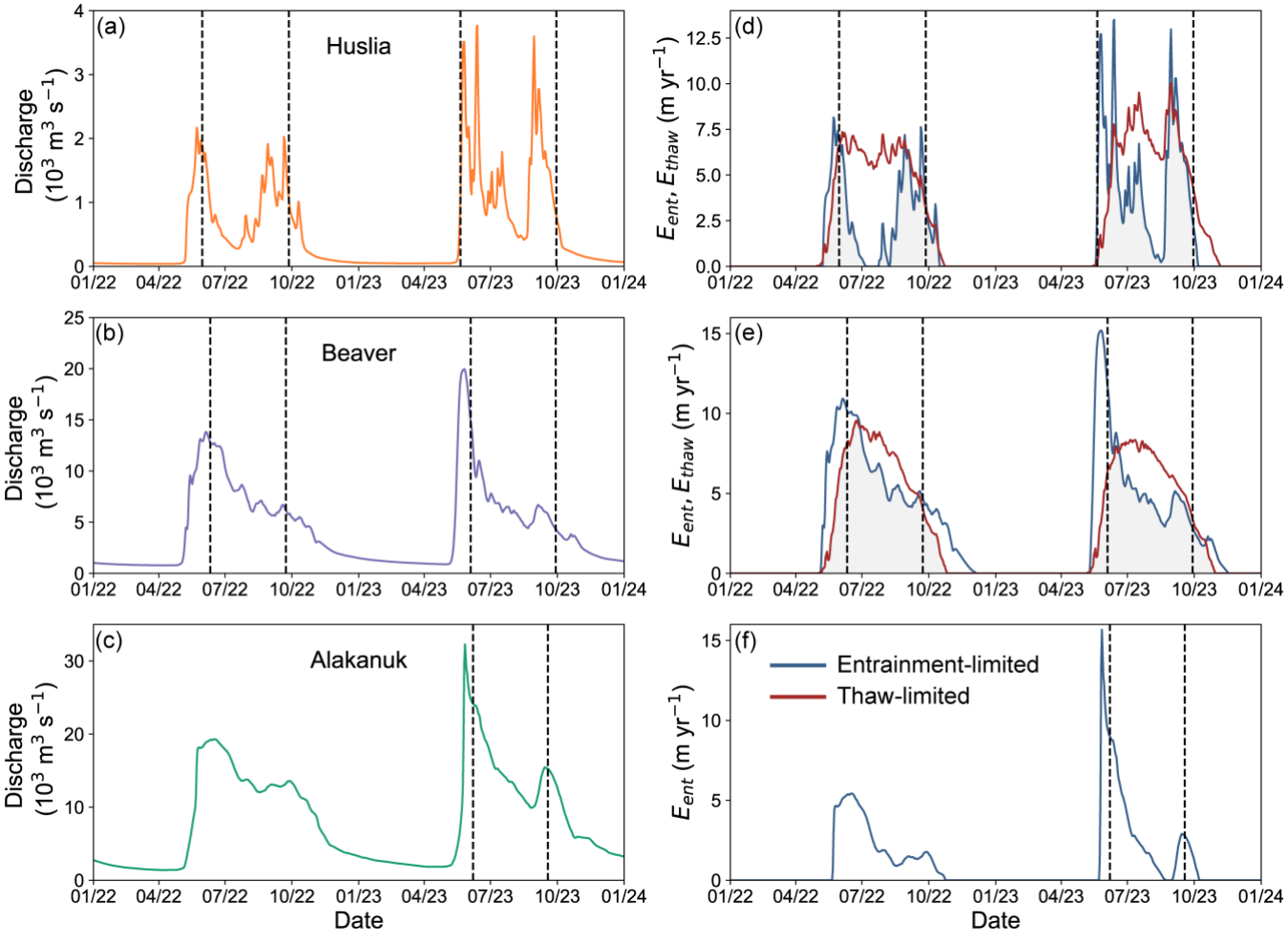


Figure 4: Hydrographs (a–c) and modeled bank erosion rates (d–f) at Hughes, Stevens Village, and Pilot Station, approximating the local timeseries at Huslia, Beaver, and Alakanuk, respectively. The dashed lines denote the timing of our sampling events on the gage hydrographs, which we approximate by offsetting the survey dates by the temporal lead (or lag) between our field site and the nearest gage station (calculated as the time needed to traverse the river distance between the field site and the gage station traveling 1 m s^{-1}). The bank erosion rates in Huslia and Beaver (d–e) are set by the minimum estimate between the entrainment- and thaw-limited erosion models. In Alakanuk, we have not observed permafrost, therefore, the erosion rates are only limited by entrainment (f).

https://doi.org/10.5194/egusphere-2026-6572
Preprint. Discussion started: 4 November 2026
© Author(s) 2026. CC BY 4.0 License.

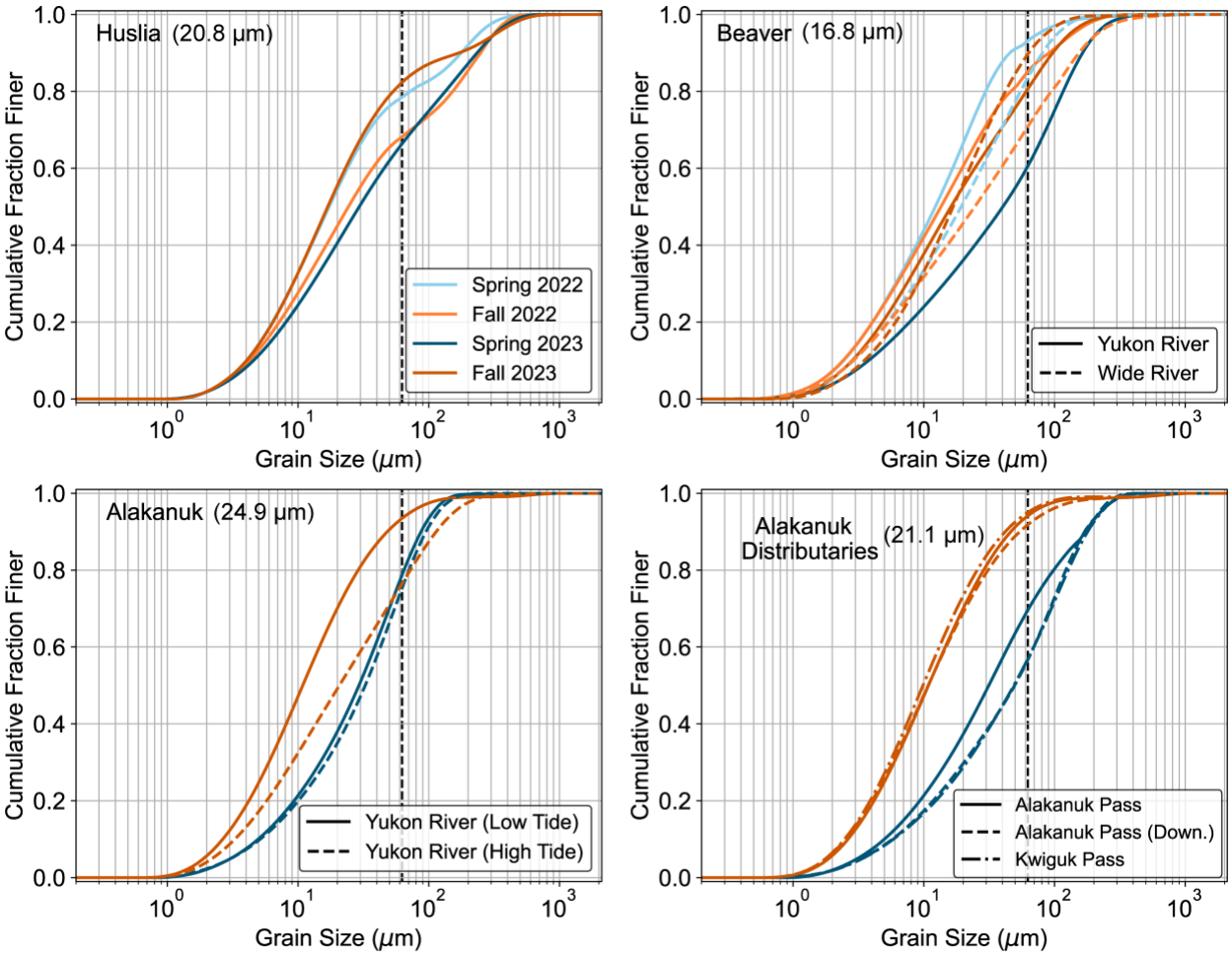


Figure 5: Depth-averaged suspended sediment grain size distributions. Depth-averaged grain size distributions were determined by numerically integrating the grain-size-specific suspended sediment concentration observed at each depth using the log-trapezoidal rule, as described in Section 3.5. For all localities, spring 2022 samples are light blue, fall 2022 samples are light orange, spring 2023 samples are dark blue, and fall 2023 samples are dark orange. In Huslia, all depth profiles were collected in the Koyukuk River. For each locality, the median D_{50} (in micrometers) is shown on each panel. The median D_{50} for all suspended sediment, spring suspended sediment, and fall suspended sediment are 19.3 µm, 30.4 µm, and 16.1 µm, respectively. The dashed black line demarcates the mud-sand boundary.

4.2 Downstream Sediment Discharge

Across all our depth profile sites, mud dominated the suspended load, as evidenced by the depth-averaged grain size distributions (Fig. 5). In Huslia, across the four seasons, the median grain size (D_{50}) of the suspended sediment in the Koyukuk River was 20.8 µm. For the Yukon River near Beaver and Alakanuk, the median D_{50} values across the sampled seasons were 16.8 and 24.9 µm, respectively. In the distributary reaches of the Yukon River, the median D_{50} value across the seasons and channels was 21.1 µm. Across the sites and years, in the spring, the median D_{50} value was 30.4 µm, coarser than the fall (16.1

https://doi.org/10.5194/egusphere-2026-6572
Preprint. Discussion started: 4 November 2026
© Author(s) 2026. CC BY 4.0 License.

μm). As observed in other localities (Nghiem et al., 2026), silt dominates the suspended sediment load of the YRB. In all cases, mud represents over half of the suspended sediment flux, and the median mud fraction was 78.8%.

From the water discharge and depth-averaged suspended sediment concentrations, we determined the total suspended sediment discharge, as well as the suspended mud discharge (Fig. 6). Depth-averaged concentrations are typically ~10^{-4} m^3 m^{-3} in the spring and ~10^{-5} m^3 m^{-3} in the fall (Text S5; Table S2), although seasonal variation is smaller in Alakanuk as compared to the other two sites. In all cases, discharge, suspended sediment concentration, and sediment discharge are higher in the spring than the fall, consistent with the hypothesis that mud concentrations are set by the flow hydraulics. On the other hand, the seasonal dynamics of the water column mud content suggest that sediment supply is also influencing amount of composition of sediment exported by the rivers of the YRB. In 2022, the water column mud fractions decreased from spring to fall in both our Huslia and Beaver sites, whereas in 2023, the water column mud fractions increased from spring to fall at all three localities. Taken together, these results suggest combined supply- and hydraulics-controlled mud discharge, as suspected for suspended bed material load. However, leaning on water column trends alone is a tenuous argument, so we provide further evidence in the forthcoming sections.

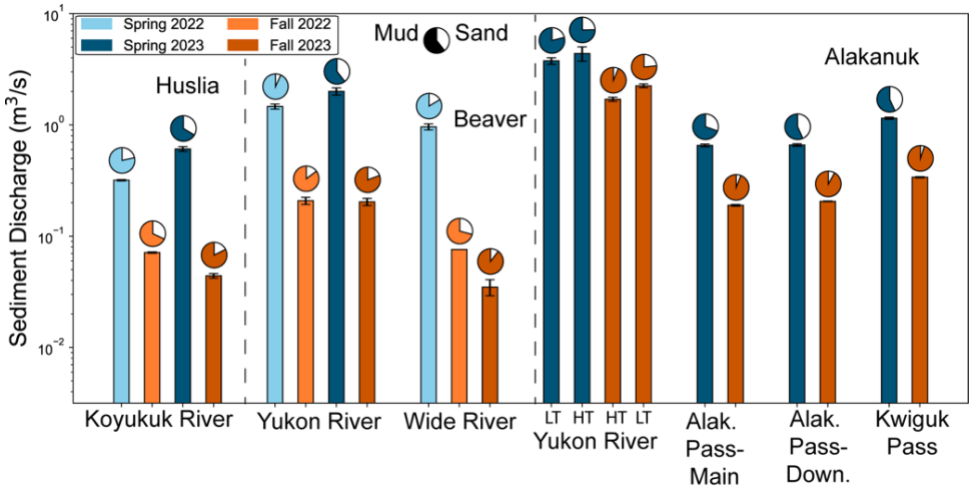


Figure 6: Seasonal sediment discharge observations across the Yukon Basin. Suspended sediment flux, the product of discharge and depth-averaged sediment concentration, is reported in cubic meters per second. Above the sediment flux, the depth averaged suspended sediment compositions are reported in pie charts. The colored and unshaded regions represent the mud and sand fractions, respectively. For the Yukon River sites near Alakanuk, the tidal phases (high tide (HT) or low tide (LT) are noted below the bars.

4.3 Evidence for Mud Flocculation

In our measured depth profiles, mud concentrations increase towards the river bed (Fig. 7a), inconsistent with the well mixed concentration-depth profile suggested by the washload hypothesis. Using our observations of the grain-size-specific suspended sediment profiles and shear velocities, we calculate grain-size-specific settling velocities for each of our depth profile sampling events. In situ mud settling velocities are consistently elevated as compared to Stokes' Law (Fig. 7b), confirming flocculation is the primary mode of transport for mud in the YRB. The median depth profile-specific floc cutoff

https://doi.org/10.5194/egusphere-2026-6572
Preprint. Discussion started: 4 November 2026
© Author(s) 2026. CC BY 4.0 License.

diameter was 32.5 μm [20, 46.25]. With the profile-specific floc cutoff diameters and the depth-averaged grain size distributions, we determined the fraction of suspended sediment finer than the floc cutoff diameter for each profile (f_f). We find the median value (n=20) of f_f to be 0.65 [0.49, 0.74]. We consider this value to be a reasonable estimate of the fraction of suspended sediment behaving as flocculated aggregates. In actuality, at every grain size class, there likely exists a distribution of in situ settling velocities, reflecting both the fractional participation in flocculation at that size class, as well as the distribution of floc diameters (Nghiem et al., 2024). However, the settling velocity recovered from the Rouse inversion reports on the bulk settling behavior of a grain size class, thus, suggesting D_{ts} is a reasonable metric by which to estimate the flocculated fraction. Considering all sediment finer than D_{ts} in each depth profile, we calculated a median in situ settling velocity of 2.86 mm s^{-1} for flocculated material in the YRB.

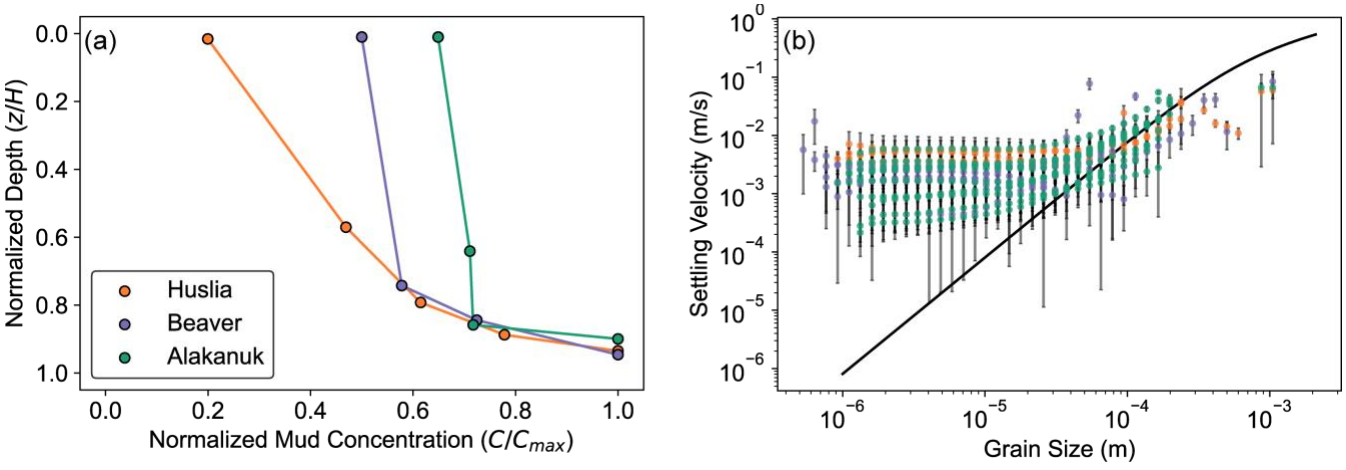


Figure 7: Mud is flocculated in the Yukon River Basin. (a) Example profiles illustrating that mud concentrations increase with depth, suggesting enhanced settling velocities of mud particles. (b) In situ settling velocities as a function of grain diameter for suspended sediment profiles collected near Huslia, Beaver, and Alakanuk. Mud settling velocities are elevated relative to Stokes' Law. In situ settling velocities are determined from fitting the Rouse-Vanoni equation (Eq. (13)) and calculating the settling velocity according to Eq. (14). The theoretical curve shows the settling velocity predicted for singular grains according to Ferguson and Church (2004). Error bars indicate 1σ uncertainty on the calculated settling velocities.

Enhanced settling velocities drastically decrease the advection length scale. For the Yukon River ($H \approx 7$ m; $U \approx 1$ m s^{-1}), enhanced settling velocities (2.86 mm s^{-1}) suggest the advection length scale for flocculated mud is about 2.5 km. In comparison, a disaggregated sediment grain at the clay–silt boundary (2 μm diameter) has an advection length scale of 2163 km and disaggregated 20 μm diameter silt grain – about the median grain size diameter of all sampled suspended sediment – has an advection length scale of 21.7 km. Thus, our in situ settling velocity estimates suggest that mud should interact with the riverbed about 10 times more frequently than would be predicted for the disaggregated, silt-dominated sediment load.

4.4 Evidence for Riverbed and Water Column Mud Exchange

Next, we look for evidence for the dynamic interchange of mud between the riverbed and water column reservoirs. First, we turn to our observations of riverbed grain size compositions (Fig. 8). If mud is behaving like washload, it should only

https://doi.org/10.5194/egusphere-2026-6572
Preprint. Discussion started: 4 November 2026
© Author(s) 2026. CC BY 4.0 License.

be present in riverbeds in exceedingly small amounts. Across all our field sites, we observe volumetrically significant mud contents in riverbeds: the median bed mud content was 10.3% [8.36, 17.5]. Our riverbed surveys are direct evidence that mud is transiently deposited in the sandy river bed. At the observed flow conditions, mud entrainment rates should be very high (de Leeuw et al., 2020), suggesting that the active layer would be rapidly stripped of mud if mud deposition rates were not balancing entrainment rates. Additionally, we highlight considerable interannual and intrannual variability in the riverbed mud content (Fig. 8), suggesting that the riverbed mud content is driven by changes in sediment supply and hydraulics, as expected for suspended bed material load that is interchanging between the bed and the water column.

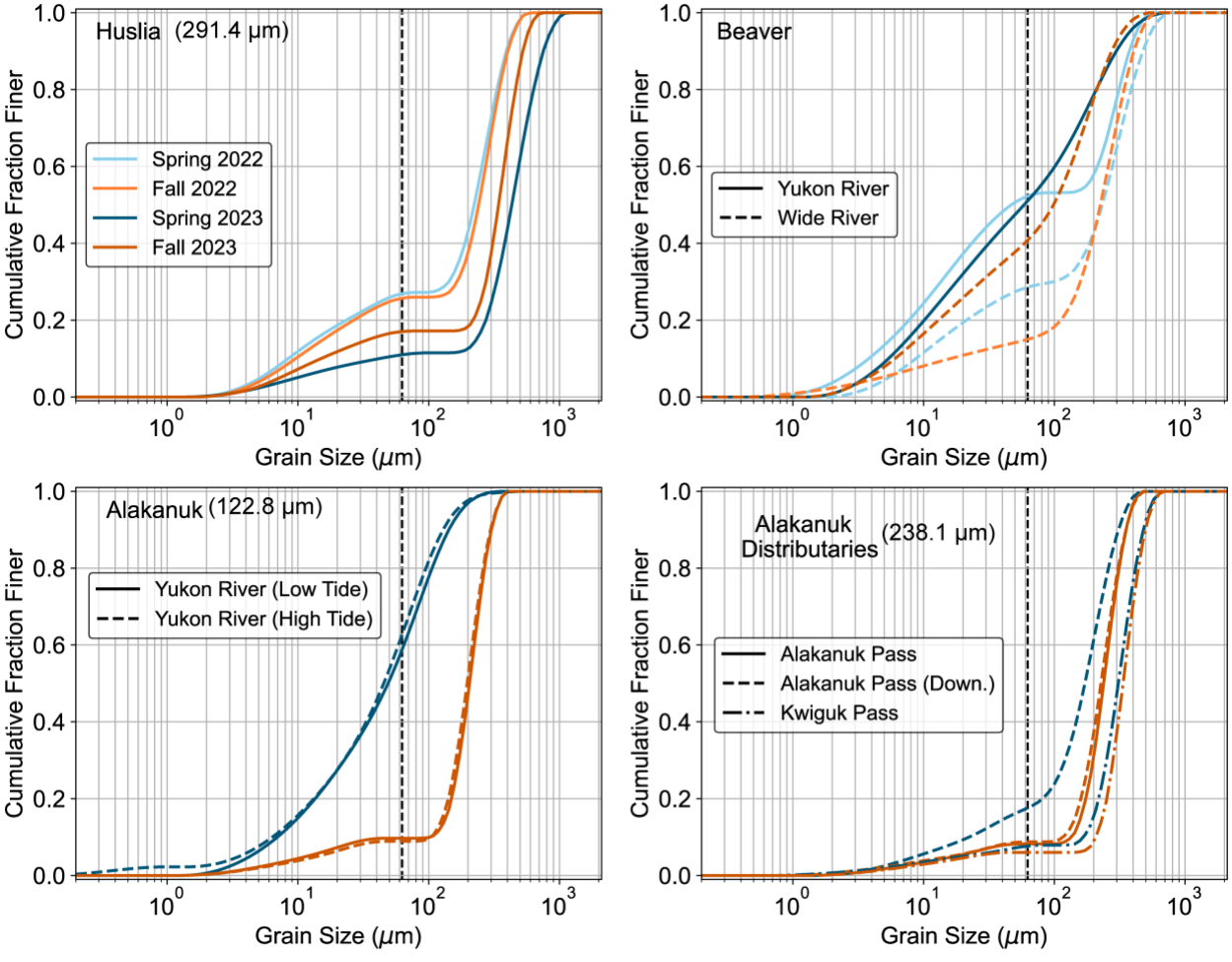


Figure 8: Bed sediment grain size distributions for each depth profile site. For all localities, spring 2022 samples are light blue, fall 2022 samples are light orange, spring 2023 samples are dark blue, and fall 2023 samples are dark orange. In Huslia, all depth profiles were collected in the Koyukuk River. For Huslia, Alakanuk, and the Alakanuk distributaries, the median D_{50} (in micrometers) is shown on each panel. The median mud fraction (f_{mud}) for all bed sediment (0.103), Huslia bed sediment (0.213), Beaver bed sediment (after correction), and Alakanuk bed sediment are 0.103, 0.213, and 0.089, respectively.

While the riverbed surveys indicate likely riverbed-water column mud exchange, a more compelling case would be made if the mud content in the bed is quantitatively as expected when entrainment is balanced by settling. To test this more

https://doi.org/10.5194/egusphere-2026-6572
Preprint. Discussion started: 4 November 2026
© Author(s) 2026. CC BY 4.0 License.

precise constraint, we compare the measured mud concentrations against predicted mud concentrations derived from entrainment models for suspended bed material. At our sites, mud concentrations are well overpredicted by entrainment theory if mud grains are assumed to be disaggregated (Fig. 9a). However, applying the entrainment theory to flocculated mud by modifying the settling velocity to be consistent with flocs (but setting the floc entrainment factor to unity in Eq. (16)) improves agreement between measured and predicted mud concentrations, supporting the hypothesis of dynamic mud interchange (Fig. 9b). Furthermore, after additionally applying the variable floc entrainment factor (Eq. 17), we observed strong agreement between the predicted and measured mud concentrations (Fig. 9c). This analysis supports the hypothesis that flocculated mud behaves like suspended bed material, thereby confirming the dynamic interchange of mud between the water column and riverbed such that entrainment and settling fluxes are near a balance. In other words, mud settling and entrainment are the two fluxes of the balanced exchange loop driving water column–riverbed mud exchange and the fact that the mud advection length scale is only a few kilometers quantitatively shows that this turnover occurs over a short stretch of river.

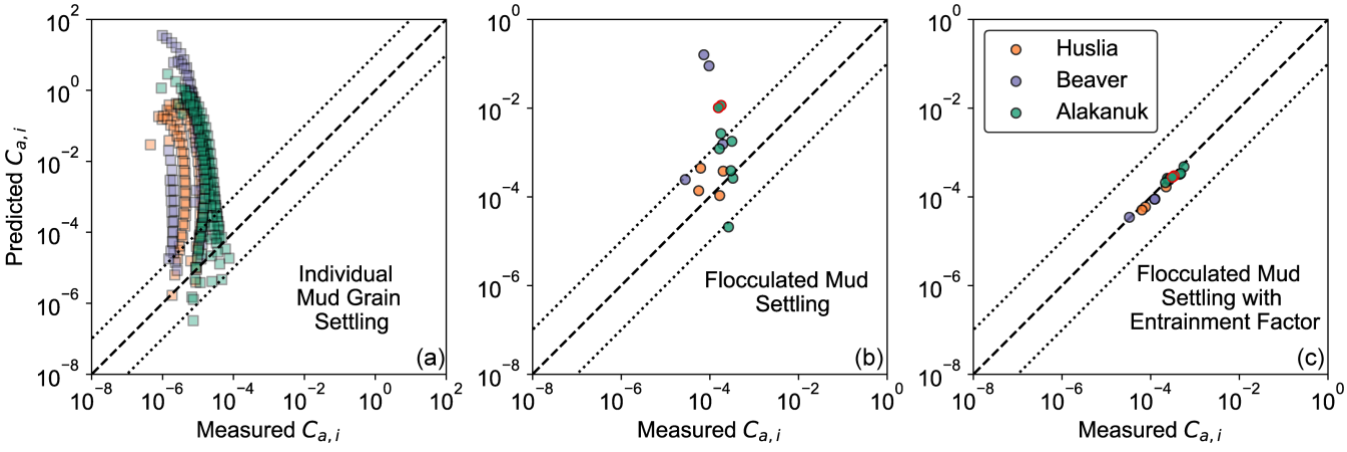


Figure 9: Comparison of measured (determined from fitting Eq. (13)) and predicted (calculated from Eqs. (15)–(16)) mud concentrations from suspended bed-material load entrainment theory. Mud settling rates are set by the diameter of disaggregated mud grains in (a). In (b) and (c) mud settling rates are set by the floc diameter. In addition, in (c), we used the variable entrainment factor (Eq. (17)), whereas it is set to unity in panel (b). The dashed and dotted lines are 1:1 and 10:1 lines, respectively. The samples outlined in red are from the springtime sampling events of the Yukon River near Alakanuk, where the bed sediment grain distribution was poorly sampled.

4.5 Evidence for Floodplain and Water Column Mud Exchange

Floodplains are commonly conceptualized as "two-layer cakes". The thicker, lower portion of the floodplain is created by the lateral accretion of point bars. The thinner upper floodplain results from the deposit of sediment during overbank floods. To interrogate floodplain–water column mud exchange, we look for the evidence of mud deposition in accreting point bars and floodplain overbank deposits, as well as mud delivery into channels by cutbank erosion of point bars and overbank deposits.

To assess mud exchange with the point bar, we rely on deposit measurements (Ke et al., 2026a) made concurrently with our suspended sediment sampling efforts. Results show that in Beaver, our sampled point bars had a median mud content

https://doi.org/10.5194/egusphere-2026-6572
Preprint. Discussion started: 4 November 2026
© Author(s) 2026. CC BY 4.0 License.

of 22%, while in Huslia the median mud content was an astonishing 64% (Fig. 10), although our bank samples are from the upper portions of point bars, which are generally believed to reflect the upward-fining of lower point bar deposits into the inclined heterolithic strata that cap point bar deposits (Bridge et al., 1995; McGowen and Garner, 1970; Thomas et al., 1987). Elevated mud content in point bars as compared to the thalweg, suggests that mud settling velocities are high enough for mud to respond to cross-sectional variations in shear stress. Overall, our findings suggest that mud is being trapped and stored in point bars as these rivers migrate laterally, supporting the hypothesis that a substantial fraction of the throughgoing mud discharge is being siphoned from the water column to the floodplain, which we will quantify through our modeling efforts. Additionally, in our sampled deposits, the mud content is essentially constant, irrespective of the age of the deposit (Text S6; Fig. S5). This observation suggests that the floodplain deposits of the Yukon River are not experiencing significant chemical weathering over the timescale of 6000–8000 years, at least insofar as the physical denudation of sediment grains is a proxy for chemical alteration in a static reservoir.

Overbank deposits on top of young, actively accreting point bars have more mud than point bars in Beaver (~32% mud) and Huslia (~91% mud; Fig. 10). Muddy overbank deposits are consistent with our water column observations; mud concentrations at the surface of the water column are about 67% of depth-averaged mud concentrations (i.e., $r_{ob,m} = 0.67$), whereas sand concentrations are about 25% of their depth-averaged values (i.e., $r_{ob,s} = 0.25$). Turning to overbank deposits in eroding cutbanks, which have experienced several millennia of overbank deposition, the deposits in Beaver are about 60% mud and the deposits in Huslia are about 85% mud (Fig. 10). Surface waters dominated by mud suggest that the water column should predominantly deliver mud to the top of the floodplain, which we confirm with our overbank granulometric observations. As with point bar growth, these results suggest that overbank deposition also transfers mud from the water column to the floodplain and each of these processes represent one-half of the water column–point bar and water column–overbank exchange loops, respectively.

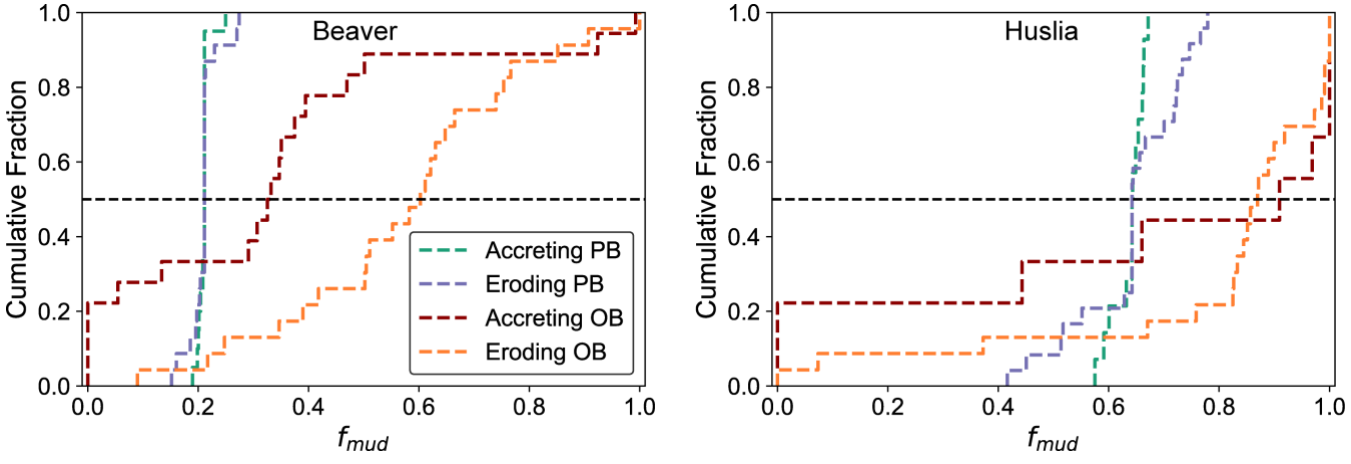


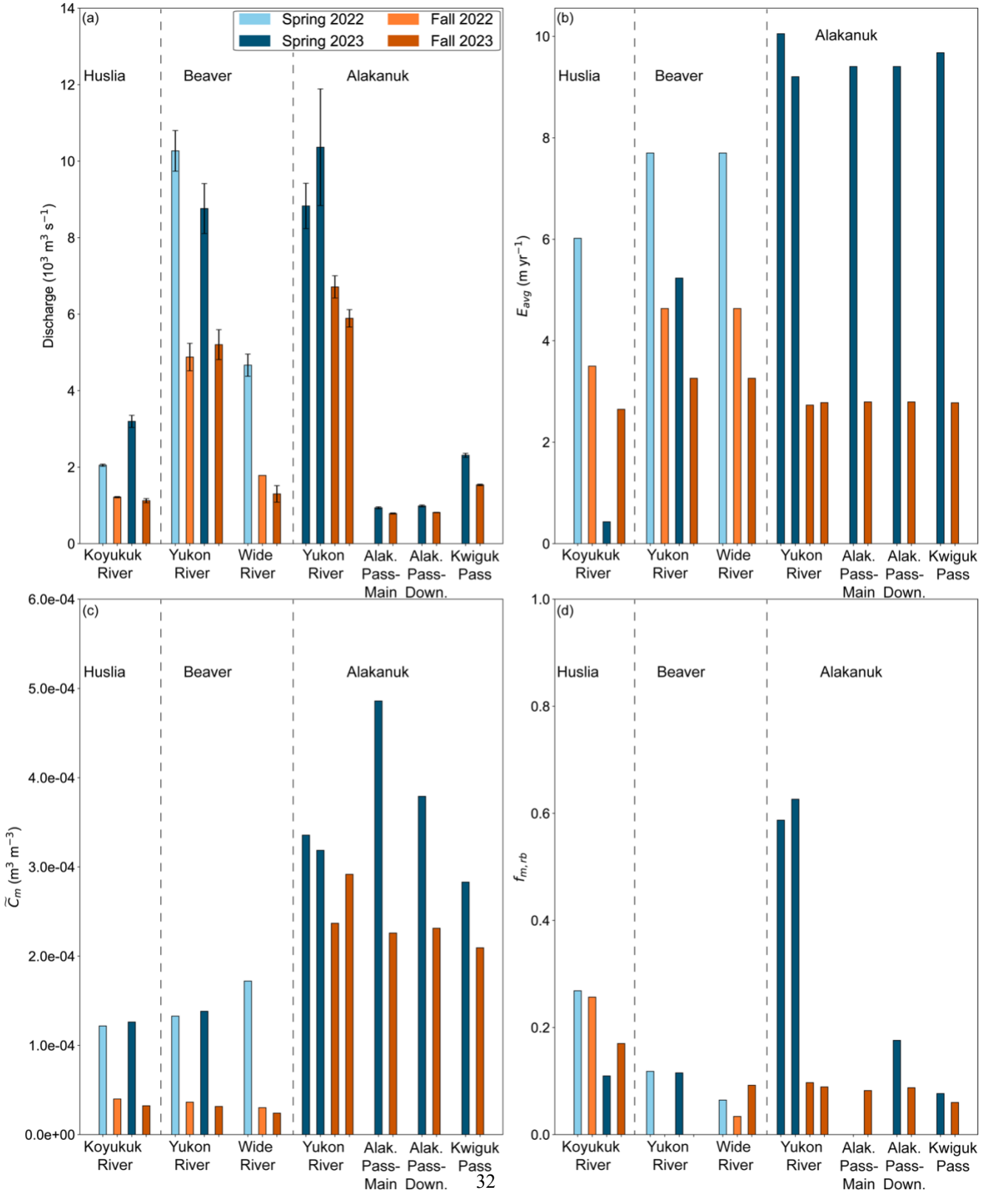
Figure 10: Mud contents of floodplain deposits in the YRB. Effective cumulative distribution functions (ECDF) of the mud content in accreting point bars and their overlying overbank deposits, as well as in eroding cutbanks, which contain old point bars and overbank deposits.

https://doi.org/10.5194/egusphere-2026-6572
Preprint. Discussion started: 4 November 2026
© Author(s) 2026. CC BY 4.0 License.

Bank erosion returns floodplain mud stored in point bar and overbank deposits back to the water column, closing the aforementioned exchange loops. Combining the mud contents of point bar (0.22) and overbank deposits (0.60) from eroding cutbanks indicates that ~30% of the sediment volume delivered by bank erosion to the channel is mud (for the Yukon, overbank deposits are about 1/6th of the total cutbank thickness). Employing an annual bank erosion rate of 2.8 m yr^{-1} along our idealized alluvial Yukon River (7 m deep, 1750 km long, point bar mud fraction of 0.211), we calculate 1.92 x 10^7 metric tons yr^{-1} of mud enter the floodplain from lateral migration, which dominates floodplain mud delivery in most years. As a point of comparison, Milliman and Farnsworth (2011) estimated the average annual Yukon River sediment flux (dominated by mud) to be 5.4 x 10^7 metric tons yr^{-1}, whereas an updated calculation from Dethier et al. (2022) estimated a higher mean annual sediment flux, 9.0 x 10^7 x 10^7 metric tons yr^{-1}. The recent estimate suggests that mud delivery to the Yukon floodplain is about 10% of the annual mud exported to the Yukon Delta, providing a quantitative estimate on the fraction of the mud flux entering the floodplain.

Bank erosion happens intermittently throughout the year, and is particularly active during floods, where mud supplied from bank erosion can overload the water column and result in increased mud contents in the riverbed. To investigate this interchange of mud from the floodplain to the river, we summarize our seasonal observations of discharge, bank erosion, mud concentration, and riverbed mud content. Given the relationship between entrainment rate and the ratio of the shear velocity to settling velocity is superlinear, $\left(u_{*sk}/w_{s,i}\right)^{1.77}$, the spring freshet should preferentially entrain fine sediment, coarsening the riverbed, which should subsequently fine throughout the summer as shear stresses drop. However, our seasonal bed sediment observations find modest to significant coarsening across seasonal measurements, despite sediment concentrations ubiquitously dropping from spring to fall, as predicted by theory (Fig. 11; Text S5). Douglas et al. (2023) predicted the rapid delivery of large slump blocks from the floodplain into the channel as a result of riverbank undercutting associated with the thawing of permafrost banks, which we observed during our field campaigns (Text S7; Fig. S6). After the freshet, bank erosion rates typically drop in response to an entrainment limitation, allowing riverbed entrainment to remove relatively fine-grained slump block material, resulting in seasonal bed sediment coarsening (Fig. 11). In fact, in the only case in which we saw seasonal bed fining (the Koyukuk River in 2023), our springtime observation occurred at the earliest outset of bank erosion while our fall observations occurred in concert with a late season bank erosion pulse. Overall, these observations indicate the mud supplied by cutbank erosion can transiently increase water column and riverbed mud concentrations, further supporting the idea that mud is in a dynamic interchange between the floodplain, water column and bed.

https://doi.org/10.5194/egusphere-2026-6572
Preprint. Discussion started: 4 November 2026
© Author(s) 2026. CC BY 4.0 License.



https://doi.org/10.5194/egusphere-2026-6572
Preprint. Discussion started: 4 November 2026
© Author(s) 2026. CC BY 4.0 License.

Figure 11: Summary of (a) discharge, (b) modeled bank erosion rates, (c) sediment concentration, and (d) bed mud content across our field sites and seasons. Notice that the bed sediment mud content does not appear to follow discharge, as is observed for the sediment concentration, but is rather influenced by the delivery of floodplain material into the channel (i.e., bank erosion rates).

4.6. Application of the Transport Model

Our field data show evidence that enhanced settling velocities due to flocculation drive a settling flux of mud to the riverbed, which is balanced in large part by the entrainment of mud. This dynamic balance necessitates some finite fraction of mud in the active layer of the riverbed to supply entrainment. Lateral migration acts to both liberate sediment from floodplains and deliver sediment back to the floodplain. Mud delivered to the channel from bank erosion may be immediately entrained or transiently stored on the riverbed as erosion acts on the newly delivered alluvium. Lastly, during overbank floods, mud is siphoned from the water column to the top of the floodplain. Given these observations, we now quantitatively evaluate the transit behavior and transit timescale of mud along the Yukon River using the statistical transport model.

https://doi.org/10.5194/egusphere-2026-6572
Preprint. Discussion started: 4 November 2026
© Author(s) 2026. CC BY 4.0 License.

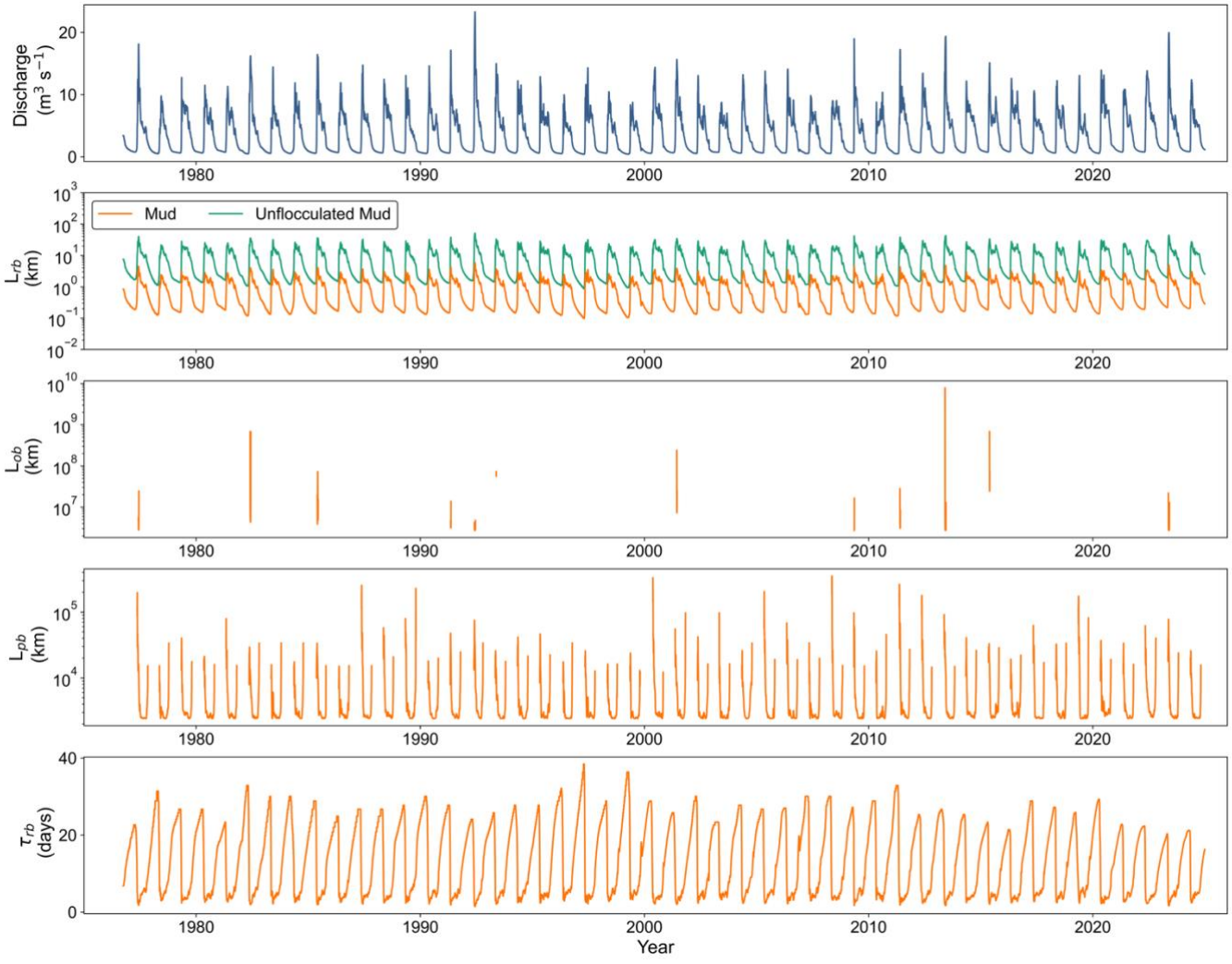


Figure 12: Time series mud characteristic transit length scales and the riverbed mud residence timescale. The length scales and timescale are calculated in accordance with the procedure described in the text. For the transit length scales, the characteristic values are determined by applying a sediment discharge-weight to the time series values. For the riverbed residence time, the characteristic values are the time-averaged values.

In Fig. 12, we present a time series of the three transit length scales and the riverbed residence timescale, which capture the time-variance in the scale factors that parametrize the exponential distributions in our transit model. These values are determined from time series of the sediment discharge and fluxes to each depositional reservoir (Text S8; Figs. S7–S8). For the riverbed, the transit length scale ($L_{rb,m}$) is shorter at low flow and longer at high flow, systematically following the hydrograph. This is because riverbed settling occurs over the river width and width does not increase linearly with discharge in rivers (Leopold and Maddock, 1953). We calculate $L_{c,rb,m}$ to be 2102 m. For overbank, smaller overbank floods have longer transit length scales ($L_{ob,m}$) than larger floods, but larger floods have a greater fractional contribution to the total sediment

https://doi.org/10.5194/egusphere-2026-6572
Preprint. Discussion started: 4 November 2026
© Author(s) 2026. CC BY 4.0 License.

discharge. We calculate $L_{c,ob,m}$ to be 5.31 x 10^9 m. For point bars, the seasonal pattern of the transit length scale ($L_{pb,m}$) is set by fluvial bank erosion rates, as well as the contribution from ice break-up. Paced solely by the thaw- and entrainment-limited migration rate, the transit length scale tends to be longer at the onset of the freshet when discharge is increasing rapidly, but bank erosion is thaw-limited. Transit length scales tend to be at their shortest in the later days of the freshet before increasing as bank erosion becomes entrainment-limited in the late summer-early fall. We calculate $L_{c,pb,m}$ to be 7.77 x 10^6 m. For the thermal and mechanical break-up scenarios, punctuated early season erosion leads to a lower transit length scale at the onset of the freshet. We calculate $L_{c,pb,m}$ to be 3.72 x 10^6 m and 3.56 x 10^6 m, respectively. Therefore, we conclude that ice break-up decreases the characteristic migration length scales by about a factor of 2, namely because it increases the migration rate. Additionally, the break-up behavior appears to be of lesser significance for our model, so we only discuss the results of the thermal break-up scenario below. Turning to the riverbed residence timescale ($\tau_{rb,m}$), we observe the same seasonal pattern as the riverbed transit length scale, however, in this case, the seasonal variation is set by the variation in the mud entrainment rate. Rapid entrainment in the ice-free season drives shorter riverbed residence of mud in comparison to the low flow winter months, wherein mud grains below the bed surface may be effectively locked in place until the subsequent freshet (Text S2). We determine $\tau_{c,rb,m}$ to be approximately 13 days, which we discuss in the context of bedform morphodynamics in Text S9.

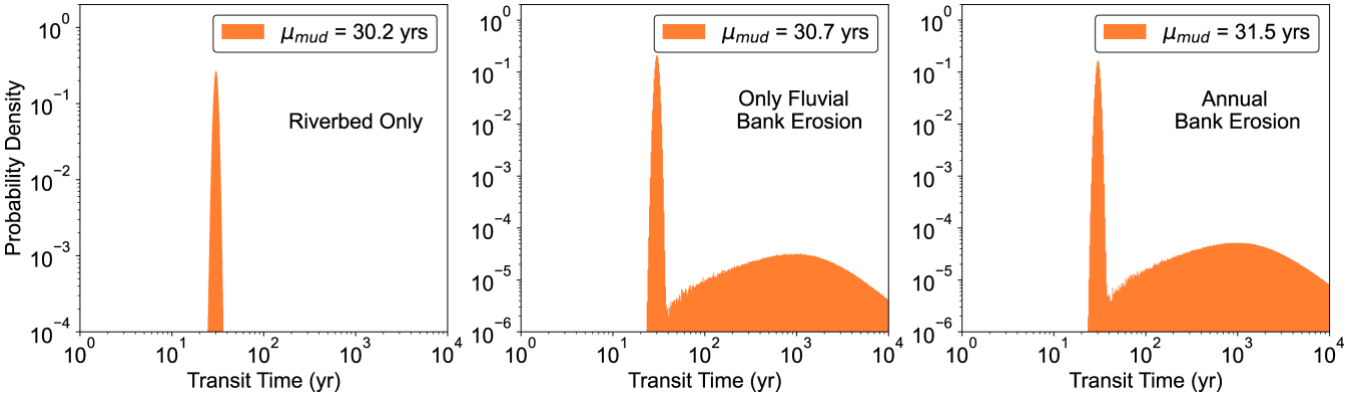


Figure 13: Simulated transit time distributions for mud experiencing (a) only riverbed deposition, (b) riverbed and floodplain deposition (lateral migration paced solely by fluvial entrainment), or (c) riverbed and floodplain deposition (annual lateral migration). Details of the model are presented in the main text.

When only riverbed storage is permitted, mud flocs have a median transit time of 30.2 years [27.8, 32.7] (5–95% quantiles), experiencing 832 depositional events (Fig. 13a). The transit time is indistinguishable from the value obtained from the analytical expression $\left(L/L_{c,rb,m}\right)\tau_{c,rb,m}$. In other words, in accordance with the central limit theorem, for a large number of sediment grains, the median transit time is equivalent to the product of the number of depositional events and the characteristic riverbed residence time. The settling velocity of mud, and hence flocculation, is particularly important for setting the transit time due to temporary bed storage. In comparison, the transit times of flocs are much greater than the case of unflocculated mud; disaggregated mud grains should transit the alluvial reach of the Yukon River in 3.42 [2.65, 4.28] years, nearly nine times less than the 30.2 years experienced by flocculated mud (Fig. S9). The median number of riverbed storage

https://doi.org/10.5194/egusphere-2026-6572
Preprint. Discussion started: 4 November 2026
© Author(s) 2026. CC BY 4.0 License.

events for unflocculated mud particles was 93, nine times fewer than those experienced by flocculated mud particles. And mud floc transit times are much longer than the water transit times through the reach (1750 km / 1 m s^{-1} ≈ 20 days), which might be assumed under the washload hypothesis.

Upon the inclusion of floodplain depositional events, the median transit time for mud particles experienced a meager increase from 30.2 years to either 30.7 years [28.0, 16403] (fluvial bank erosion only) or 31.5 years [28.2, 35847] (fluvial and ice-mediated erosion; Fig. 13b–c). Our observations suggest that for mud particles, floodplain interactions are sufficiently rare such that the *median* mud transit time is well approximated by a model that only considers riverbed deposition. However, a significant but minority fraction of mud grains (~20–40%) experienced floodplain storage, significantly increasing the *mean* transit time (Fig. 14). For mud particles experiencing floodplain storage, typical transit times range from several centuries to millennia. Once particles entered floodplain storage, their cumulative transit time was controlled by meander kinetics, as articulated in Geyman et al. (2025).

While our focus here is on mud, model results for sand are a useful point of comparison. Considering only riverbed deposition, sand particles have a median transit time of 851 [831, 872] years, experiencing 9329 depositional events (Text S10; Fig. S9). Longer transit times for sand particles is the direct result of a shorter characteristic transit length scale (i.e., more storage events) and a longer riverbed residence time (i.e., longer storage events). In contrast to mud, sand transit times increased from 851 years to 5647 years [840, 65202] when thaw- and entrainment-limited lateral migration was considered and 21455 years [861, 99048] when the observed annual migration was considered (Fig. S10). Therefore, sand transit times are dominated by floodplain storage as predicted by previous workers (e.g., Torres et al., 2017; Geyman et al., 2025), although riverbed storage remains non-negligible and can be predicted by the same analytical expression as mud.

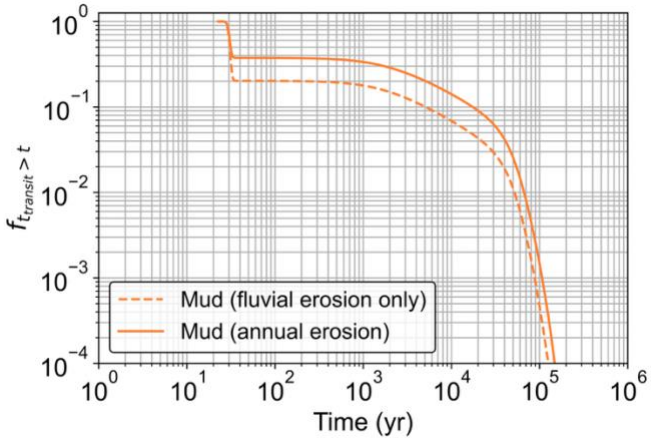


Figure 14: The fraction of simulated mud transit times longer than time, *t*. The magnitude of the initial drop in each survivorship curve is the fraction of mud particles that never interacted with the floodplain. Following floodplain deposition, the transit time curve mirrors the floodplain survival curve.

https://doi.org/10.5194/egusphere-2026-6572
Preprint. Discussion started: 4 November 2026
© Author(s) 2026. CC BY 4.0 License.

5 Discussion

5.1 How Mud is Transported

Historical inquiry into the global mud cycle was centered on the export of mud to the coastal oceans (Holeman, 1968; Milliman and Farnsworth, 2011; Milliman and Meade, 1983; Syvitski et al., 2003). Given that mud was conceptualized as washload, quantifying riverine export was considered a difficult accounting problem, and understanding the controls on sediment delivery to channels was the foremost question (Milliman and Syvitski, 1992). In recent decades, efforts have expanded to consider the deposition of mud into long-term continental reservoirs (i.e., lakes and floodplains), as well as the effects of dam emplacement and anthropogenically enhanced soil erosion (for a review of recent developments, see Bianchi et al., 2024). However, given that these efforts are budget-focused, they have largely ignored the transport history of mud.

Concurrently, efforts to understand the transport history of floodplain sediments has led to the development of geochemical tracers that estimate sediment transit times by inventorying storage time-dependent tracers along a river reach. For example, U-series isotopes potentially provide a chronometer for the mud comminution age, the time since mineral grains were reduced to <63 μm in size (DePaolo et al., 2006). However, because mud grains are created predominantly by chemical weathering on hillslopes (Yoo et al., 2009) rather than in-channel comminution (Jerolmack and Brzinski, 2010), the comminution age is the sum of the hillslope storage and alluvial transit, requiring knowledge of hillslope residence times to determine alluvial transit times. Additionally, results from Martin et al. (2019) suggest comminution ages are highly sensitive to the chosen uranium leaching rate. Alternatively, Repasch et al. (2020) measured depth-integrated meteoric ^{10}Be, a cosmogenic nuclide that coats the surface of sediment grains during prolonged exposure to meteoric precipitation, along the Rio Bermejo. Given that all suspended grains are inventoried, the method reports on the mean sediment transit time, which our results suggest is an intermediate value between a spectrum of grain-size-specific transit time distributions. As grain size increases, a greater fraction of sediment in a given grain size class enters floodplain transit, progressively evolving the grain-size-specific transit time distribution from a normal distribution controlled by the number and residence time of riverbed depositional events (i.e., centered at $\left(L/L_{c,rb,i}\right)\tau_{c,rb,i}$) to a normal distribution controlled by the typical number of floodplain depositional events and the residence time of floodplain depositional events (i.e., the convolution of the floodplain storage time distribution).

Our grain-size-specific sediment budget approach suggests that for fine sediment, median transit times are approximated by cumulative riverbed storage times. In turn, cumulative riverbed storage times for these particles are approximated by the product of the number of river storage events and the characteristic riverbed storage timescale. We find that mud particles in the Yukon River are cycled in and out of the riverbed hundreds of times before reaching the coast, extending the concept of land-to-ocean loops in the global land (Bianchi et al., 2024) and carbon cycles (Regnier et al., 2022; Fig. 15). In addition, our observations and calculations show that a minor, yet meaningful portion of the river mud discharge enters floodplain storage (centennial storage is common), generally consistent with budget-based estimates at the global scale (Bianchi et al., 2024).

https://doi.org/10.5194/egusphere-2026-6572
Preprint. Discussion started: 4 November 2026
© Author(s) 2026. CC BY 4.0 License.

Freshwater flocculation is ubiquitous in rivers (Lamb et al., 2020a), suggesting that mud advection length scales are on the order of 1-100 km in Earth's large rivers. In the Yukon River, we found that the characteristic riverbed mud residence timescale, which is set by the dune height, riverbed mud content, and mud entrainment rate, is about 10 days. Dune heights and mud entrainment rates in the Yukon River are typical of large alluvial rivers, therefore, assuming the riverbed mud content observed in the Yukon is not anomalous, decadal mud transit times should be common, implying that the fate and transport of organic carbon (Hilton et al., 2024), particle-scavenged metals (Horowitz, 1985), and anthropogenic pollutants (Chiaia-Hernández et al., 2022) are impacted by transient riverbed storage. With proper calibration, the burgeoning efforts to measure suspended sediment concentrations from satellite imagery (e.g., Dethier et al., 2022; Tian et al., 2026) could be used to quantify mud entrainment rates when paired with grain size distributions at reach scales (Gilbert, 2025). Thus, a future exists wherein mud transit times are estimated at scale, improving our understanding of the transport history of mud, organic carbon, and pollutants globally.

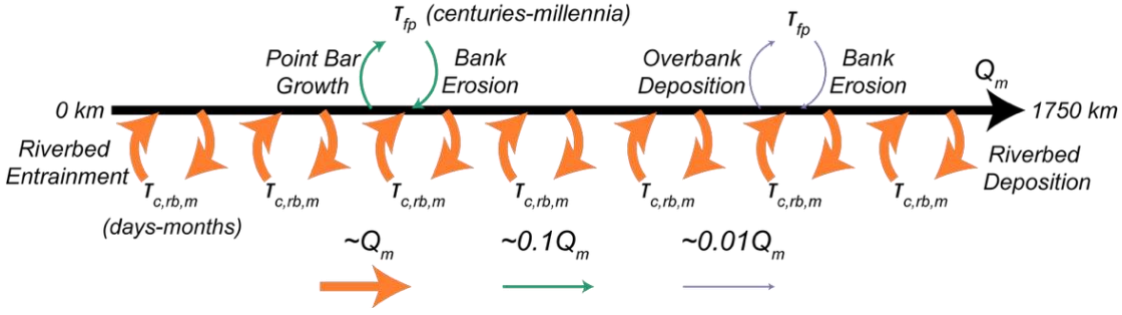


Figure 15: Schematic of mud transport in the Yukon River Basin. Mud grains are deposited and entrained from the riverbed over 800 times before reaching the coastal ocean. Individual riverbed residence times are typically days-weeks but may extend to months in ephemeral or cryosphere rivers. In aggregate, riverbed storage results in annual-decadal storage times for mud particles. In addition to the numerous riverbed depositional events, a subset of mud particles also experience floodplain deposition, extending their residence time in terrestrial landscapes from decades to centuries, or even millennia.

5.2 How POC is Transported

Particulate organic carbon in river systems is strongly associated with the mud fraction of mineral sediment (Bouchez et al., 2014; Galy et al., 2008; Ke et al., 2022). Given that we found that much of the mud is flocculated in the Yukon River, which has also been demonstrated in other rivers (Lamb et al., 2020b; Nghiem et al., 2026; Osborn et al., 2023), we hypothesize that POC transport may follow similar mud-floc dynamics in which interchange between the water column, bed and floodplain dramatically increase the residence time of POC in river corridors owing to transient storage. Indeed, tracer experiments conducted on fine particulate organic matter (~10-1000 µm; ~1.2-2.0 kg m^{-3}) observed organic matter transport to be governed by the same transport hop dynamics as suspended sediment (Cushing et al., 1993; Miller and Georgian, 1992; Webster et al., 1999), supporting the extension of our conceptual framework to sediment-associated organic carbon. Furthermore, organic material has been shown to be important in causing mud to flocculate in freshwater rivers (Nghiem et al., 2022). Further, flocs have been observed to deposit onto riverbeds, transport as saltating bedload, and evolve dynamically in size and density in

https://doi.org/10.5194/egusphere-2026-6572
Preprint. Discussion started: 4 November 2026
© Author(s) 2026. CC BY 4.0 License.

riverbed environments (Schieber et al., 2007; Baas et al., 2015; Tran and Strom, 2019; Wysocki and Hajek, 2021; de Lange et al., 2024).

Following our observation that median mud transit times are dominated by riverbed residence, most floc-associated POC should also spend its time in the riverbed, suggesting that the riverbed may be the locus for organic carbon respiration, rather than water column or floodplain environments. This suggestion is consistent with riverine CO_2 source allocation models, which highlight subsurface respiration within the benthic, hyporheic, and riparian zones as a dominant source of emitted CO_2 in the rivers of the continental United States (Butman and Raymond, 2011; Kirk and Cohen, 2023; Saccardi et al., 2024). Further, because the sediment-transport active layer is a constantly shifting environment overlain by an oxygen-saturated water column, aerobic respiration may predominate in this environment, in stark contrast to static, saturated floodplain soils, wherein anoxia is a predictable feature of the landscape (Boye et al., 2017). If so, the active layer of the riverbed may be a unique, O_2-replete zone wherein carbon degradation proceeds rapidly. Once mud-associated organic carbon is delivered to more static reservoirs in the coastal environment, it is possible that the remineralization rates drop orders of magnitude in response to the O_2-limitation (Hartnett et al., 1998), just as they do in floodplain deposits (Ke et al., 2026b).

By depositing mud and organic carbon into point bar deposits, flocculation may stabilize transiently stored floodplain carbon. In the Yukon River Basin, previous workers found that POC delivered to point bars is rendered functionally inaccessible as a byproduct of the anoxic, frozen, and mineral-replete conditions (Ke et al., 2026b). In the absence of flocculation, mud, and therefore organic carbon, would be more enriched in overbank deposits, which experience more favorable conditions for microbial decomposition. In lower latitude environments, flocculation-enhanced floodplain POC storage could result in the in-place incineration of biospheric organic carbon by microbes over floodplain storage timescales, particularly for regions of floodplains above the water table (Scheingross et al., 2021).

Lastly, the constant interchange of water column POC with a decadal-scale POC reservoir contradicts the idea that dynamic seasonal erosion signals can be ascertained from suspended sediment time series. Long-term records of POC composition in six major Arctic rivers support this hypothesis, finding near complete overlap in the isotopic and molecular composition of POC between seasons (McClelland et al., 2016; Behnke et al., 2023). In other words, water column-riverbed exchange acts to diffuse temporally discrete sediment delivery pulses into channels. Particularly in rivers with highly variable discharge (i.e., monsoon- or freshet-dominated hydrographs), resuspension of previously deposited riverbed material should mix POC signals from prior transport events. Similarly, strategic seasonal sampling to avoid autochthonous aquatic carbon (e.g., Galy and Eglinton, 2011), should be approached with caution, albeit contribution from aquatic biomass may remain negligible.

5.3 Transport Dynamics in a Changing Arctic

As the climate warms, hydrologic intensification is expected to increase water discharge across the Arctic (Beel et al., 2021). For example, historical hydrologic analysis of the Yukon River (Ge et al., 2013) found an 8.0% increase in annual discharge from 1977–2006. Increasing discharge should increase both the characteristic riverbed transit length scale and the

https://doi.org/10.5194/egusphere-2026-6572
Preprint. Discussion started: 4 November 2026
© Author(s) 2026. CC BY 4.0 License.

characteristic riverbed residence timescale, altering the characteristic behavior of transport hops and storage events. However, the quantitative effect on the median riverbed residence time depends on the adjustment of river hydrologic geometries to increased discharge. In addition to hydrologic intensification, accelerated thaw (Chadburn et al., 2017) should accelerate the denudation of mountainous terrain, increasing the amount of sediment transported by large cryosphere rivers (Li et al., 2021). Concurrently, Arctic rivers are simultaneously experiencing waning ice break-up intensities, decreasing the break-up erosion pulse, and accelerated floodplain permafrost thaw, increasing fluvial entrainment rates by lifting the thaw-limitation on bank erosion (Geyman and Lamb, 2026). Rivers experiencing a slowdown in lateral migration over the last few decades (such as the Yukon River) have erosion budgets dominated by break-up erosion, whereas rivers experiencing accelerated migration are dominated by coupled thaw- and entrainment-limited erosion. For rivers experiencing accelerated bank erosion rates, low-lying lands left in the wake of lateral migration should, if at least transiently, increase the amount of sediment and carbon deposited in overbank. In addition, if increases in river discharge correspond to increases in freshet discharge, overbank deposition rates should further increase. On the other hand, rivers experiencing slower migration rates should experience decreased overbank deposition fluxes, albeit the effects of decreased migration are potentially offset by increases in peak discharge. In both cases, the consequence of Arctic warming on river-corridor mud residence times depends on the quantitative balance between the changes in sediment discharge, bank erosion rates, and overbank deposition rates (e.g., increases in sediment discharge where accompanied by increases in bank erosion rates in the Canadian Arctic; Fields et al., 2025).

6 Conclusions

In the Yukon River, we observed that mud is flocculated, settling at rates on the order of 1 mm s^{-1}, and is actively exchanging between the water column, riverbed and floodplain. Evidence for this interchange includes: 1) enhanced mud settling velocities, 2) high riverbed mud contents, 3) balanced mud entrainment and deposition, and 4) high mud contents in point bars and overbank deposits.

Building upon our field observations, a statistical transit model indicates that mud flocs have typical transport lengths of about 2 km and storage times of about 13 days in these environments. Integrating the model across the lower 1750 km of the Yukon River, we found that 60–80% of mud flocs transit the reach of the Yukon River in about 30 years, depositing over 800 times in the riverbed. Therefore, these mud grains spend over 99% of the transit time in the active layer of the riverbed. The remaining 20–40% of mud particles experience one floodplain depositional event, in addition to riverbed storage, increasing the transit time for those particles from about three decades to centuries, or even millennia. In all cases, transit times are much longer than the ~20 days predicted if mud particles were to follow the water under the washload paradigm.

Consequently, mud-associated carbon, metals, and pollutants should all spend significant time in the active layer of riverbeds or both riverbeds and floodplains. Our results imply that riverbeds are likely to be important locations for organic carbon respiration in alluvial systems. Future work focusing on respiration dynamics in this transient storage environment, particularly in evolving Arctic environments, should prove insightful for constraining and predicting riverine greenhouse gas

https://doi.org/10.5194/egusphere-2026-6572
Preprint. Discussion started: 4 November 2026
© Author(s) 2026. CC BY 4.0 License.

emissions. Furthermore, the evolution of sediment discharge, bank erosion rates, and overbank flood frequencies and magnitudes in a warming Arctic will all influence the transport and storage of POC.

Code and data availability

The data and code needed to run the transit model are available via Zenodo at https://doi.org/10.5281/zenodo.23547497. Suspended sediment concentrations and grain size statistics, as well as riverbed grain size statistics are available via the NSF Arctic Data Center (https://doi.org/10.18739/A22Z12R5X). Floodplain grain size distributions are also archived in the NSF Arctic Data Center (https://doi.org/10.18739/A28G8FK7W). The river discharge data from the USGS gauge at Stevens Village is available for download from the National Water Dashboard: https://dashboard.waterdata.usgs.gov/app/nwd/en/.

Author contributions

Conceptualization: J.S.A. and M.P.L. Methodology: J.S.A and M.P.L. Investigation: J.S.A., Y.K., E.C.G., J.A.N., J.N.R., and A.L.G. Formal Analysis: J.S.A. Visualization: J.S.A. Supervision: A.J.W., W.W.F., and M.P.L. Writing—Original Draft: J.S.A. Writing—Reviewing and Editing: J.S.A., Y.K., E.C.G., J.A.N., J.N.R., A.L.G, M.I.S., J.S.M., A.J.W., W.W.F., M.P.L.

Competing interests

At least one of the (co-)authors is a member of the editorial board of Earth Surface Dynamics.

https://doi.org/10.5194/egusphere-2026-6572
Preprint. Discussion started: 4 November 2026
© Author(s) 2026. CC BY 4.0 License.

Acknowledgements

We thank the Huslia, Beaver, and Alakanuk tribal and village councils for river and land access and the Yukon River Inter-Tribal Watershed Council for logistical support. We thank A. Attla, D. Dayton, S. Huffman, K. Vanderpool, R. Williams, C. Wiehl, J. Isidore, P. Phillips Jr., R. Stanislaus, and J. Stronghearts for river navigation and expertise. We also thank R. Blankenship, M. Douglas, K. Dunne, H. Dion-Kirschner, E. Mutter, E. Seelen for help in the field and N. Dalleska for laboratory assistance.

Financial support

This work was supported by NSF award 2127442 and Caltech's Resnick Sustainability Institute. J. Anadu was supported by the NSF Graduate Research Fellowship Program (award 2139433) and the NASA Future Investigators in NASA Earth and Space Science and Technology Program (award 80NSSC23K1560).

References

Anadu, J., Ke, Y., Douglas, M., Li, G., Giuntoni, A., Chadwick, A., Dunne, K., Geyman, E., Kemeny, P., Magyar, J., Mutter, E., Nghiem, J., Piliouras, A., Reahl, J., Rowland, J., Seelen, E., Schwenk, J., Smith, M. I., Fischer, W., West, A. J., and Lamb, M.: Suspended and bed sediment grain size distributions at three riverine sites in the Yukon River Watershed: Alakanuk, Beaver, and Huslia (Alaska) (2018-2023), https://doi.org/10.18739/A22Z12R5X, 2025.

Arcement, G. J. and Schneider, V. R.: Guide for selecting Manning's roughness coefficients for natural channels and flood plains, Water Supply Paper, 2339, U.S. G.P.O. ; For sale by the Books and Open-File Reports Section, U.S. Geological Survey, https://doi.org/10.3133/wsp2339, 1989.

Baas, J. H., Best, J. L., and Peakall, J.: Predicting bedforms and primary current stratification in cohesive mixtures of mud and sand, Journal of the Geological Society, 173, 12–45, https://doi.org/10.1144/jgs2015-024, 2015.

Battin, T. J., Lauerwald, R., Bernhardt, E. S., Bertuzzo, E., Gener, L. G., Hall, R. O., Hotchkiss, E. R., Maavara, T., Pavelsky, T. M., Ran, L., Raymond, P., Rosentreter, J. A., and Regnier, P.: River ecosystem metabolism and carbon biogeochemistry in a changing world, Nature, 613, 449–459, https://doi.org/10.1038/s41586-022-05500-8, 2023.

Beel, C. R., Heslop, J. K., Orwin, J. F., Pope, M. A., Schevers, A. J., Hung, J. K. Y., Lafrenière, M. J., and Lamoureux, S. F.: Emerging dominance of summer rainfall driving High Arctic terrestrial-aquatic connectivity, Nat Commun, 12, 1448, https://doi.org/10.1038/s41467-021-21759-3, 2021.

https://doi.org/10.5194/egusphere-2026-6572
Preprint. Discussion started: 4 November 2026
© Author(s) 2026. CC BY 4.0 License.

Behnke, M. I., Tank, S. E., McClelland, J. W., Holmes, R. M., Haghipour, N., Eglinton, T. I., Raymond, P. A., Suslova, A., Zhulidov, A. V., Gurtovaya, T., Zimov, N., Zimov, S., Mutter, E. A., Amos, E., and Spencer, R. G. M.: Aquatic biomass is a major source to particulate organic matter export in large Arctic rivers, Proceedings of the National Academy of Sciences, 120, e2209883120, https://doi.org/10.1073/pnas.2209883120, 2023.

Bianchi, T. S., Mayer, L. M., Amaral, J. H. F., Arndt, S., Galy, V., Kemp, D. B., Kuehl, S. A., Murray, N. J., and Regnier, P.: Anthropogenic impacts on mud and organic carbon cycling, Nat. Geosci., 17, 287–297, https://doi.org/10.1038/s41561-024-01405-5, 2024.

Blair, N. E. and Aller, R. C.: The Fate of Terrestrial Organic Carbon in the Marine Environment, Annual Review of Marine Science, 4, 401–423, https://doi.org/10.1146/annurev-marine-120709-142717, 2012.

Blair, N. E., Leithold, E. L., and Aller, R. C.: From bedrock to burial: the evolution of particulate organic carbon across coupled watershed-continental margin systems, Marine Chemistry, 92, 141–156, https://doi.org/10.1016/j.marchem.2004.06.023, 2004.

Bock, M. J. and Mayer, L. M.: Mesodensity organo–clay associations in a near-shore sediment, Marine Geology, 163, 65–75, https://doi.org/10.1016/S0025-3227(99)00105-X, 2000.

Bolin, B. and Rodhe, H.: A note on the concepts of age distribution and transit time in natural reservoirs, Tellus, 25, 58–62, https://doi.org/10.1111/j.2153-3490.1973.tb01594.x, 1973.

Bouchez, J., Galy, V., Hilton, R. G., Gaillardet, J., Moreira-Turcq, P., Pérez, M. A., France-Lanord, C., and Maurice, L.: Source, transport and fluxes of Amazon River particulate organic carbon: Insights from river sediment depth-profiles, Geochimica et Cosmochimica Acta, 133, 280–298, https://doi.org/10.1016/j.gca.2014.02.032, 2014.

Boye, K., Noël, V., Tfaily, M. M., Bone, S. E., Williams, K. H., Bargar, J. R., and Fendorf, S.: Thermodynamically controlled preservation of organic carbon in floodplains, Nature Geosci, 10, 415–419, https://doi.org/10.1038/ngeo2940, 2017.

Brabets, T. A., Wang, B., and Meade, R. H.: Environmental and hydrologic overview of the Yukon River basin, Alaska and Canada | U.S. Geological Survey, Water-Resources Investigations Report, https://doi.org/10.3133/wri994204, 2000.

Bradley, D. N. and Tucker, G. E.: The storage time, age, and erosion hazard of laterally accreted sediment on the floodplain of a simulated meandering river, Journal of Geophysical Research: Earth Surface, 118, 1308–1319, https://doi.org/10.1002/jgrf.20083, 2013.

Bradley, R. W. and Venditti, J. G.: Reevaluating dune scaling relations, Earth-Science Reviews, 165, 356–376, https://doi.org/10.1016/j.earscirev.2016.11.004, 2017.

Bridge, J. S., Alexander, J., Collier, R. E. Ll., Gawthorpe, Rob. L., and Jarvis, J.: Ground-penetrating radar and coring used to study the large-scale structure of point-bar deposits in three dimensions, Sedimentology, 42, 839–852, https://doi.org/10.1111/j.1365-3091.1995.tb00413.x, 1995.

Brousse, G., Liébault, F., Arnaud-Fassetta, G., and Vazquez-Tarrio, D.: Experimental bed active-layer survey with active RFID scour chains: Example of two braided rivers (the Drac and the Vénéon) in the French Alps, E3S Web Conf., 40, 04016, https://doi.org/10.1051/e3sconf/20184004016, 2018.

Butman, D. and Raymond, P. A.: Significant efflux of carbon dioxide from streams and rivers in the United States, Nature Geosci, 4, 839–842, https://doi.org/10.1038/ngeo1294, 2011.

https://doi.org/10.5194/egusphere-2026-6572
Preprint. Discussion started: 4 November 2026
© Author(s) 2026. CC BY 4.0 License.

Chadburn, S. E., Burke, E. J., Cox, P. M., Friedlingstein, P., Hugelius, G., and Westermann, S.: An observation-based constraint on permafrost loss as a function of global warming, Nature Clim Change, 7, 340–344, https://doi.org/10.1038/nclimate3262, 2017.

Chiaia-Hernández, A. C., Casado-Martinez, C., Lara-Martin, P., and Bucheli, T. D.: Sediments: sink, archive, and source of contaminants, Environ Sci Pollut Res Int, 29, 85761–85765, https://doi.org/10.1007/s11356-022-24041-1, 2022.

Church, M. and Haschenburger, J. K.: What is the "active layer"?, Water Resources Research, 53, 5–10, https://doi.org/10.1002/2016WR019675, 2017.

Churchman, G. J., Singh, M., Schapel, A., Sarkar, B., and Bolan, N.: Clay Minerals as the Key to the Sequestration of Carbon in Soils, Clays and Clay Minerals, 68, 135–143, https://doi.org/10.1007/s42860-020-00071-z, 2020.

Clement, D. T.: Fluvial geomorphology of the Yukon River, Yukon Flats, Alaska, https://doi.org/10.11575/PRISM/22783, 1999.

Constantine, J. A., Dunne, T., Ahmed, J., Legleiter, C., and Lazarus, E. D.: Sediment supply as a driver of river meandering and floodplain evolution in the Amazon Basin, Nature Geosci, 7, 899–903, https://doi.org/10.1038/ngeo2282, 2014.

Curry, K. J., Bennett, R. H., Mayer, L. M., Curry, A., Abril, M., Biesiot, P. M., and Hulbert, M. H.: Direct visualization of clay microfabric signatures driving organic matter preservation in fine-grained sediment, Geochimica et Cosmochimica Acta, 71, 1709–1720, https://doi.org/10.1016/j.gca.2007.01.009, 2007.

Cushing, C. E., Minshall, G. W., and Newbold, J. D.: Transport dynamics of fine particulate organic matter in two Idaho streams, Limnology and Oceanography, 38, 1101–1115, https://doi.org/10.4319/lo.1993.38.6.1101, 1993.

DePaolo, D. J., Maher, K., Christensen, J. N., and McManus, J.: Sediment transport time measured with U-series isotopes: Results from ODP North Atlantic drift site 984, Earth and Planetary Science Letters, 248, 394–410, https://doi.org/10.1016/j.epsl.2006.06.004, 2006.

Dethier, E. N., Renshaw, C. E., and Magilligan, F. J.: Rapid changes to global river suspended sediment flux by humans, Science, 376, 1447–1452, https://doi.org/10.1126/science.abn7980, 2022.

Dosseto, A., Bourdon, B., and Turner, S. P.: Uranium-series isotopes in river materials: Insights into the timescales of erosion and sediment transport, Earth and Planetary Science Letters, 265, 1–17, https://doi.org/10.1016/j.epsl.2007.10.023, 2008.

Douglas, M. M., Li, G. K., Fischer, W. W., Rowland, J. C., Kemeny, P. C., West, A. J., Schwenk, J., Piliouras, A. P., Chadwick, A. J., and Lamb, M. P.: Organic carbon burial by river meandering partially offsets bank erosion carbon fluxes in a discontinuous permafrost floodplain, Earth Surface Dynamics, 10, 421–435, https://doi.org/10.5194/esurf-10-421-2022, 2022.

Douglas, M. M., Dunne, K. B. J., and Lamb, M. P.: Sediment Entrainment and Slump Blocks Limit Permafrost Riverbank Erosion, Geophysical Research Letters, 50, e2023GL102974, https://doi.org/10.1029/2023GL102974, 2023.

Dunne, K. B. J., Nittrouer, J. A., Abolfazli, E., Osborn, R., and Strom, K. B.: Hydrodynamically-Driven Deposition of Mud in River Systems, Geophysical Research Letters, 51, e2023GL107174, https://doi.org/10.1029/2023GL107174, 2024.

Eke, E., Parker, G., and Shimizu, Y.: Numerical modeling of erosional and depositional bank processes in migrating river bends with self-formed width: Morphodynamics of bar push and bank pull, Journal of Geophysical Research: Earth Surface, 119, 1455–1483, https://doi.org/10.1002/2013JF003020, 2014.

https://doi.org/10.5194/egusphere-2026-6572
Preprint. Discussion started: 4 November 2026
© Author(s) 2026. CC BY 4.0 License.

Faust, J. C., Tessin, A., Fisher, B. J., Zindorf, M., Papadaki, S., Hendry, K. R., Doyle, K. A., and März, C.: Millennial scale persistence of organic carbon bound to iron in Arctic marine sediments, Nat Commun, 12, 275, https://doi.org/10.1038/s41467-020-20550-0, 2021.

Ferguson, R. I. and Church, M.: A Simple Universal Equation for Grain Settling Velocity, Journal of Sedimentary Research, 74, 933–937, https://doi.org/10.1306/051204740933, 2004.

Fettweis, M., Belliard, J.-P., Silori, S., Terseleer, N., Tran, D., Delhaye, L., Amadei Martinez, L., Brun, A., Sabbe, K., De Rijcke, M., Lee, B. J., Riethmüller, R., Shen, X., Verney, R., Ha, H. K., and Desmit, X.: Suspended particulate matter along the land–ocean continuum, Nat Rev Earth Environ, 1–17, https://doi.org/10.1038/s43017-026-00815-w, 2026.

Fields, J., Kreisler, J., Dethier, E., Perrotti, J., and Renshaw, C.: Fluvial erosion linked to warming in the Canadian Arctic, Commun Earth Environ, 6, 267, https://doi.org/10.1038/s43247-025-02234-z, 2025.

Fredsøe, J. and Deigaard, R.: Mechanics of Coastal Sediment Transport, World Scientific Publishing Company, 390 pp., 1992.

Friedlingstein, P., O'Sullivan, M., Jones, M. W., Andrew, R. M., Bakker, D. C. E., Hauck, J., Landschützer, P., Le Quéré, C., Li, H., Luijkx, I. T., Peters, G. P., Peters, W., Pongratz, J., Schwingshackl, C., Sitch, S., Canadell, J. G., Ciais, P., Aas, K., Alin, S. R., Anthoni, P., Barbero, L., Bates, N. R., Bellouin, N., Benoit-Cattin, A., Berghoff, C. F., Bernardello, R., Bopp, L., Brasika, I. B. M., Chamberlain, M. A., Chandra, N., Chevallier, F., Chini, L. P., Collier, N. O., Colligan, T. H., Cronin, M., Djeutchouang, L. M., Dou, X., Enright, M. P., Enyo, K., Erb, M., Evans, W., Feely, R. A., Feng, L., Ford, D. J., Foster, A., Fransner, F., Gasser, T., Gehlen, M., Gkritzalis, T., Goncalves De Souza, J., Grassi, G., Gregor, L., Gruber, N., Guenet, B., Gürses, Ö., Harrington, K., Harris, I., Heinke, J., Hurtt, G. C., Iida, Y., Ilyina, T., Ito, A., Jacobson, A. R., Jain, A. K., Jarníková, T., Jersild, A., Jiang, F., Jones, S. D., Kato, E., Keeling, R. F., Klein Goldewijk, K., Knauer, J., Kong, Y., Korsbakken, J. I., Koven, C., Kunimitsu, T., Lan, X., Liu, J., Liu, Z., Liu, Z., Lo Monaco, C., Ma, L., Marland, G., McGuire, P. C., McKinley, G. A., Melton, J. R., Monacci, N., Monier, E., Morgan, E. J., Munro, D. R., Müller, J. D., Nakaoka, S.-I., Nayagam, L. R., Niwa, Y., Nutzel, T., Olsen, A., Omar, A. M., Pan, N., Pandey, S., Pierrot, D., Qin, Z., Regnier, P., Rehder, G., Resplandy, L., Roobaert, A., Rosan, T. M., Rödenbeck, C., Schwinger, J., Skjelvan, I., Smallman, T. L., Spada, V., Sreeush, M. G., Sun, Q., Sutton, A. J., Sweeney, C., Swingedouw, D., Séférian, R., Takao, S., Tatebe, H., Tian, H., Tian, X., Tilbrook, B., Tsujino, H., Tubiello, F., van Ooijen, E., van der Werf, G. R., van de Velde, S. J., Walker, A. P., Wanninkhof, R., Yang, X., Yuan, W., Yue, X., and Zeng, J.: Global Carbon Budget 2025, Earth System Science Data, 18, 3211–3288, https://doi.org/10.5194/essd-18-3211-2026, 2026.

Galy, V. and Eglinton, T.: Protracted storage of biospheric carbon in the Ganges–Brahmaputra basin, Nature Geosci, 4, 843–847, https://doi.org/10.1038/ngeo1293, 2011.

Galy, V., France-Lanord, C., and Lartiges, B.: Loading and fate of particulate organic carbon from the Himalaya to the Ganga–Brahmaputra delta, Geochimica et Cosmochimica Acta, 72, 1767–1787, https://doi.org/10.1016/j.gca.2008.01.027, 2008.

Ganti, V., Lamb, M. P., and McElroy, B.: Quantitative bounds on morphodynamics and implications for reading the sedimentary record, Nat Commun, 5, 3298, https://doi.org/10.1038/ncomms4298, 2014.

Ge, S., Yang, D., and Kane, D. L.: Yukon River Basin long-term (1977–2006) hydrologic and climatic analysis, Hydrological Processes, 27, 2475–2484, https://doi.org/10.1002/hyp.9282, 2013.

Georgiou, K., Jackson, R. B., Vindušková, O., Abramoff, R. Z., Ahlström, A., Feng, W., Harden, J. W., Pellegrini, A. F. A., Polley, H. W., Soong, J. L., Riley, W. J., and Torn, M. S.: Global stocks and capacity of mineral-associated soil organic carbon, Nat Commun, 13, 3797, https://doi.org/10.1038/s41467-022-31540-9, 2022.

https://doi.org/10.5194/egusphere-2026-6572
Preprint. Discussion started: 4 November 2026
© Author(s) 2026. CC BY 4.0 License.



Geyman, E. C. and Lamb, M. P.: Resolving the changing pace of Arctic rivers, Nat. Clim. Chang., 16, 77–86, https://doi.org/10.1038/s41558-025-02512-w, 2026.

Geyman, E. C., Douglas, M. M., Avouac, J.-P., and Lamb, M. P.: Permafrost slows Arctic riverbank erosion, Nature, 634, 359–365, https://doi.org/10.1038/s41586-024-07978-w, 2024.

Geyman, E. C., Ke, Y., Magyar, J. S., Reahl, J. N., Soldano, V., Brown, N. D., West, A. J., Fischer, W. W., and Lamb, M. P.: Scaling laws for sediment storage and turnover in river floodplains, Science Advances, 11, eadu8574, https://doi.org/10.1126/sciadv.adu8574, 2025.

Gilbert, J. T.: An extrapolation algorithm for estimating river bed grain size distributions across basins, Earth Surface Dynamics, 13, 1307–1317, https://doi.org/10.5194/esurf-13-1307-2025, 2025.

Graf, W. H. and Cellino, M.: Suspension flows in open channels; experimental study, Journal of Hydraulic Research, 40, 435–447, https://doi.org/10.1080/00221680209499886, 2002.

Granet, M., Chabaux, F., Stille, P., Dosseto, A., France-Lanord, C., and Blaes, E.: U-series disequilibria in suspended river sediments and implication for sediment transfer time in alluvial plains: The case of the Himalayan rivers, Geochimica et Cosmochimica Acta, 74, 2851–2865, https://doi.org/10.1016/j.gca.2010.02.016, 2010.

Handley, H. K., Turner, S., Afonso, J. C., Dosseto, A., and Cohen, T.: Sediment residence times constrained by uranium-series isotopes: A critical appraisal of the comminution approach, Geochimica et Cosmochimica Acta, 103, 245–262, https://doi.org/10.1016/j.gca.2012.10.047, 2013.

Hartnett, H. E., Keil, R. G., Hedges, J. I., and Devol, A. H.: Influence of oxygen exposure time on organic carbon preservation in continental margin sediments, Nature, 391, 572–575, https://doi.org/10.1038/35351, 1998.

Haschenburger, J. K.: A Probability model of scour and fill depths in gravel-bed channels, Water Resources Research, 35, 2857–2869, https://doi.org/10.1029/1999WR900153, 1999.

Hemingway, J. D., Rothman, D. H., Grant, K. E., Rosengard, S. Z., Eglinton, T. I., Derry, L. A., and Galy, V. V.: Mineral protection regulates long-term global preservation of natural organic carbon, Nature, 570, 228–231, https://doi.org/10.1038/s41586-019-1280-6, 2019.

Hilton, R. G., Schwab, M., and Galy, V.: Dynamics of particulate organic carbon mobilization, storage, and export across river sedimentary systems, 3rd ed., Elsevier, 2024.

Holeman, J. N.: The Sediment Yield of Major Rivers of the World, Water Resources Research, 4, 737–747, https://doi.org/10.1029/WR004i004p00737, 1968.

Horowitz, A. J.: A primer on trace metal-sediment chemistry, Water Supply Paper, 2277, U.S. G.P.O., https://doi.org/10.3133/wsp2277, 1985.

Jerolmack, D. J. and Brzinski, T. A., III: Equivalence of abrupt grain-size transitions in alluvial rivers and eolian sand seas: A hypothesis, Geology, 38, 719–722, https://doi.org/10.1130/G30922.1, 2010.

Ke, Y., Calmels, D., Bouchez, J., and Quantin, C.: MOdern River archivEs of Particulate Organic Carbon: MOREPOC, Earth System Science Data, 14, 4743–4755, https://doi.org/10.5194/essd-14-4743-2022, 2022.

https://doi.org/10.5194/egusphere-2026-6572
Preprint. Discussion started: 4 November 2026
© Author(s) 2026. CC BY 4.0 License.

Ke, Y., Reahl, J., Anadu, J., Douglas, M., Dunne, K., Geyman, E., Magyar, J., Mutter, E., Norton, A., Smith, I., Fischer, W., West, A. J., and Lamb, M.: Grain Size Distribution in the Subsurface Sediments of Floodplains Across the Yukon River Basin, Alaska, 2022, https://doi.org/10.18739/A28G8FK7W, 2026a.

Ke, Y., West, A. J., Geyman, E. C., Huy, K. A., Dion-Kirschner, H., Smith, M. I., Anadu, J. S., Magyar, J. S., Lamb, M. P., and Fischer, W. W.: Persistent organic carbon storage in river floodplains over millennia, Nat Commun, 17, 5794, https://doi.org/10.1038/s41467-026-72405-9, 2026b.

Keiluweit, M., Wanzek, T., Kleber, M., Nico, P., and Fendorf, S.: Anaerobic microsites have an unaccounted role in soil carbon stabilization, Nat Commun, 8, 1771, https://doi.org/10.1038/s41467-017-01406-6, 2017.

Kirk, L. and Cohen, M. J.: River Corridor Sources Dominate CO2 Emissions From a Lowland River Network, Journal of Geophysical Research: Biogeosciences, 128, e2022JG006954, https://doi.org/10.1029/2022JG006954, 2023.

Kleber, M., Bourg, I. C., Coward, E. K., Hansel, C. M., Myneni, S. C. B., and Nunan, N.: Dynamic interactions at the mineral–organic matter interface, Nat Rev Earth Environ, 2, 402–421, https://doi.org/10.1038/s43017-021-00162-y, 2021.

Lamb, M. P., McElroy, B., Kopriva, B., Shaw, J., and Mohrig, D.: Linking river-flood dynamics to hyperpycnal-plume deposits: Experiments, theory, and geological implications, GSA Bulletin, 122, 1389–1400, https://doi.org/10.1130/B30125.1, 2010.

Lamb, M. P., de Leeuw, J., Fischer, W. W., Moodie, A. J., Venditti, J. G., Nittrouer, J. A., Haught, D., and Parker, G.: Mud in rivers transported as flocculated and suspended bed material, Nat. Geosci., 13, 566–570, https://doi.org/10.1038/s41561-020-0602-5, 2020a.

Lamb, M. P., de Leeuw, J., Fischer, W. W., Moodie, A. J., Venditti, J. G., Nittrouer, J. A., Haught, D., and Parker, G.: Mud in rivers transported as flocculated and suspended bed material, Nat. Geosci., 13, 566–570, https://doi.org/10.1038/s41561-020-0602-5, 2020b.

de Lange, S. I., van der Wilk, A., Chassagne, C., Ali, W., Born, M. P., Brodersen, K., Hoitink, A. J. F., and Waldschläger, K.: Migrating subaqueous dunes capture clay flocs, Commun Earth Environ, 5, 729, https://doi.org/10.1038/s43247-024-01901-x, 2024.

Lauer, J. W. and Parker, G.: Modeling framework for sediment deposition, storage, and evacuation in the floodplain of a meandering river: Theory, Water Resources Research, 44, https://doi.org/10.1029/2006WR005528, 2008a.

Lauer, J. W. and Parker, G.: Net local removal of floodplain sediment by river meander migration, Geomorphology, 96, 123–149, https://doi.org/10.1016/j.geomorph.2007.08.003, 2008b.

de Leeuw, J., Lamb, M. P., Parker, G., Moodie, A. J., Haught, D., Venditti, J. G., and Nittrouer, J. A.: Entrainment and suspension of sand and gravel, Earth Surface Dynamics, 8, 485–504, https://doi.org/10.5194/esurf-8-485-2020, 2020.

Leopold, L. B. and Maddock, T.: The Hydraulic Geometry of Stream Channels and Some Physiographic Implications, U.S. Government Printing Office, 68 pp., 1953.

Li, D., Lu, X., Overeem, I., Walling, D. E., Syvitski, J., Kettner, A. J., Bookhagen, B., Zhou, Y., and Zhang, T.: Exceptional increases in fluvial sediment fluxes in a warmer and wetter High Mountain Asia, Science, 374, 599–603, https://doi.org/10.1126/science.abi9649, 2021.

https://doi.org/10.5194/egusphere-2026-6572
Preprint. Discussion started: 4 November 2026
© Author(s) 2026. CC BY 4.0 License.

Limaye, A. B. S. and Lamb, M. P.: A vector-based method for bank-material tracking in coupled models of meandering and landscape evolution, Journal of Geophysical Research: Earth Surface, 118, 2421–2437, https://doi.org/10.1002/2013JF002854, 2013.

Lininger, K. B., Wohl, E., Rose, J. R., and Leisz, S. J.: Significant Floodplain Soil Organic Carbon Storage Along a Large High-Latitude River and its Tributaries, Geophysical Research Letters, 46, 2121–2129, https://doi.org/10.1029/2018GL080996, 2019.

Lupker, M., France-Lanord, C., Lavé, J., Bouchez, J., Galy, V., Métivier, F., Gaillardet, J., Lartiges, B., and Mugnier, J.-L.: A Rouse-based method to integrate the chemical composition of river sediments: Application to the Ganga basin, Journal of Geophysical Research: Earth Surface, 116, https://doi.org/10.1029/2010JF001947, 2011.

Martin, A. N., Dosseto, A., May, J.-H., Jansen, J. D., Kinsley, L. P. J., and Chivas, A. R.: Sediment residence times in catchments draining to the Gulf of Carpentaria, northern Australia, inferred by uranium comminution dating, Geochimica et Cosmochimica Acta, 244, 264–291, https://doi.org/10.1016/j.gca.2018.09.031, 2019.

Martin, H. K., Edmonds, D. A., and Lewis, Q. W.: Four Years of Meander-Bend Evolution Captured by Drone-Based Lidar Reveals Lack of Width Maintenance on the White River, Indiana, USA, Journal of Geophysical Research: Earth Surface, 129, e2023JF007574, https://doi.org/10.1029/2023JF007574, 2024.

Mason, J. and Mohrig, D.: Using Time-Lapse Lidar to Quantify River Bend Evolution on the Meandering Coastal Trinity River, Texas, USA, Journal of Geophysical Research: Earth Surface, 123, 1133–1144, https://doi.org/10.1029/2017JF004492, 2018.

Mason, J. and Mohrig, D.: Differential bank migration and the maintenance of channel width in meandering river bends, Geology, 47, 1136–1140, https://doi.org/10.1130/G46651.1, 2019.

McClelland, J. W., Holmes, R. M., Peterson, B. J., Raymond, P. A., Striegl, R. G., Zhulidov, A. V., Zimov, S. A., Zimov, N., Tank, S. E., Spencer, R. G. M., Staples, R., Gurtovaya, T. Y., and Griffin, C. G.: Particulate organic carbon and nitrogen export from major Arctic rivers, Global Biogeochemical Cycles, 30, 629–643, https://doi.org/10.1002/2015GB005351, 2016.

McGowen, J. H. and Garner, L. E.: Physiographic Features and Stratification Types of Coarse-Grained Pointbars: Modern and Ancient Examples, Sedimentology, 14, 77–111, https://doi.org/10.1111/j.1365-3091.1970.tb00184.x, 1970.

Middelburg, J. J.: Marine Carbon Biogeochemistry: A Primer for Earth System Scientists, Springer International Publishing, Cham, https://doi.org/10.1007/978-3-030-10822-9, 2019.

Miller, J. and Georgian, T.: Estimation of Fine Particulate Transport in Streams Using Pollen as a Seston Analog, Journal of the North American Benthological Society, https://doi.org/10.2307/1467383, 1992.

Milliman, J. D. and Farnsworth, K. L.: River Discharge to the Coastal Ocean: A Global Synthesis, Cambridge University Press, Cambridge, https://doi.org/10.1017/CBO9780511781247, 2011.

Milliman, J. D. and Meade, R. H.: World-Wide Delivery of River Sediment to the Oceans, The Journal of Geology, 91, 1–21, https://doi.org/10.1086/628741, 1983.

Milliman, J. D. and Syvitski, J. P. M.: Geomorphic/Tectonic Control of Sediment Discharge to the Ocean: The Importance of Small Mountainous Rivers, The Journal of Geology, 100, 525–544, https://doi.org/10.1086/629606, 1992.

https://doi.org/10.5194/egusphere-2026-6572
Preprint. Discussion started: 4 November 2026
© Author(s) 2026. CC BY 4.0 License.

Nghiem, J. A., Fischer, W. W., Li, G. K., and Lamb, M. P.: A Mechanistic Model for Mud Flocculation in Freshwater Rivers, Journal of Geophysical Research: Earth Surface, 127, e2021JF006392, https://doi.org/10.1029/2021JF006392, 2022.

Nghiem, J. A., Li, G. K., Harringmeyer, J. P., Salter, G., Fichot, C. G., Cortese, L., and Lamb, M. P.: Testing floc settling velocity models in rivers and freshwater wetlands, Earth Surface Dynamics, 12, 1267–1294, https://doi.org/10.5194/esurf-12-1267-2024, 2024.

Nghiem, J. A., Li, G. K., Harringmeyer, J. P., Salter, G., Fichot, C. G., Wright, K., Passalacqua, P., and Lamb, M. P.: Evidence for Mud as Flocculated Bed-Material Load Versus Washload in a River Delta, Journal of Geophysical Research: Earth Surface, 130, e2025JF008366, https://doi.org/10.1029/2025JF008366, 2025.

Nghiem, J. A., Li, G. K., Zepeda-Rosales, M., Li, Y., and Lamb, M. P.: Flocculated Silt, Not Clay, Dominates River Suspended Sediment Load, Geophysical Research Letters, 53, e2025GL118655, https://doi.org/10.1029/2025GL118655, 2026.

Osborn, R., Dunne, K. B. J., Ashley, T., Nittrouer, J. A., and Strom, K.: The Flocculation State of Mud in the Lowermost Freshwater Reaches of the Mississippi River: Spatial Distribution of Sizes, Seasonal Changes, and Their Impact on Vertical Concentration Profiles, Journal of Geophysical Research: Earth Surface, 128, e2022JF006975, https://doi.org/10.1029/2022JF006975, 2023.

Paola, C. and Voller, V. R.: A generalized Exner equation for sediment mass balance, Journal of Geophysical Research: Earth Surface, 110, https://doi.org/10.1029/2004JF000274, 2005.

Parker, G., Garcia, M., Fukushima, Y., and Yu, W.: Experiments on turbidity currents over an erodible bed, Journal of Hydraulic Research, https://doi.org/10.1080/00221688709499292, 1987.

Parker, G., Shimizu, Y., Wilkerson, G. V., Eke, E. C., Abad, J. D., Lauer, J. W., Paola, C., Dietrich, W. E., and Voller, V. R.: A new framework for modeling the migration of meandering rivers, Earth Surface Processes and Landforms, 36, 70–86, https://doi.org/10.1002/esp.2113, 2011.

Pizzuto, J. E.: Long-term storage and transport length scale of fine sediment: Analysis of a mercury release into a river, Geophysical Research Letters, 41, 5875–5882, https://doi.org/10.1002/2014GL060722, 2014.

Pizzuto, J. E. and Li, C. X.: On The Advective Velocity of Washload in a Typical Gravel-bedded River, AGU Fall Meeting Abstracts, EP53D-1527, 2024.

Rahuel, J. L., Holly, F. M., Chollet, J. P., Belleudy, P. J., and Yang, G.: Modeling of Riverbed Evolution for Bedload Sediment Mixtures, Journal of Hydraulic Engineering, 115, 1521–1542, https://doi.org/10.1061/(ASCE)0733-9429(1989)115:11(1521), 1989.

Recking, A.: An analysis of nonlinearity effects on bed load transport prediction, Journal of Geophysical Research: Earth Surface, 118, 1264–1281, https://doi.org/10.1002/jgrf.20090, 2013.

Regnier, P., Resplandy, L., Najjar, R. G., and Ciais, P.: The land-to-ocean loops of the global carbon cycle, Nature, 603, 401–410, https://doi.org/10.1038/s41586-021-04339-9, 2022.

Repasch, M., Wittmann, H., Scheingross, J. S., Sachse, D., Szupiany, R., Orfeo, O., Fuchs, M., and Hovius, N.: Sediment Transit Time and Floodplain Storage Dynamics in Alluvial Rivers Revealed by Meteoric 10Be, Journal of Geophysical Research: Earth Surface, 125, e2019JF005419, https://doi.org/10.1029/2019JF005419, 2020.

https://doi.org/10.5194/egusphere-2026-6572
Preprint. Discussion started: 4 November 2026
© Author(s) 2026. CC BY 4.0 License.

Repasch, M., Scheingross, J. S., Hovius, N., Lupker, M., Wittmann, H., Haghipour, N., Gröcke, D. R., Orfeo, O., Eglinton, T. I., and Sachse, D.: Fluvial organic carbon cycling regulated by sediment transit time and mineral protection, Nat. Geosci., 14, 842–848, https://doi.org/10.1038/s41561-021-00845-7, 2021.

Rickenmann, D. and Recking, A.: Evaluation of flow resistance in gravel-bed rivers through a large field data set, Water Resources Research, 47, https://doi.org/10.1029/2010WR009793, 2011.

Rouse, H.: Modern Conceptions of the Mechanics of Fluid Turbulence, Transactions of the American Society of Civil Engineers, 102, 463–505, https://doi.org/10.1061/TACEAT.0004872, 1937.

Saccardi, B., Brinkerhoff, C. B., Gleason, C. J., and Winnick, M. J.: Toward Modeling Continental-Scale Inland Water Carbon Dioxide Emissions, AGU Advances, 5, e2024AV001294, https://doi.org/10.1029/2024AV001294, 2024.

Scheingross, J. S., Repasch, M. N., Hovius, N., Sachse, D., Lupker, M., Fuchs, M., Halevy, I., Gröcke, D. R., Golombek, N. Y., Haghipour, N., Eglinton, T. I., Orfeo, O., and Schleicher, A. M.: The fate of fluvially-deposited organic carbon during transient floodplain storage, Earth and Planetary Science Letters, 561, 116822, https://doi.org/10.1016/j.epsl.2021.116822, 2021.

Schieber, J., Southard, J., and Thaisen, K.: Accretion of Mudstone Beds from Migrating Floccule Ripples, Science, 318, 1760–1763, https://doi.org/10.1126/science.1147001, 2007.

Schiller, B. and Strom, K.: Entrainment of Muddy Sediment From Immobile Gravel River Beds, Water Resources Research, 62, e2025WR041519, https://doi.org/10.1029/2025WR041519, 2026.

Schuur, E. a. G., McGuire, A. D., Schädel, C., Grosse, G., Harden, J. W., Hayes, D. J., Hugelius, G., Koven, C. D., Kuhry, P., Lawrence, D. M., Natali, S. M., Olefeldt, D., Romanovsky, V. E., Schaefer, K., Turetsky, M. R., Treat, C. C., and Vonk, J. E.: Climate change and the permafrost carbon feedback, Nature, 520, 171–179, https://doi.org/10.1038/nature14338, 2015.

Schuur, E. A. G., Abbott, B. W., Commane, R., Ernakovich, J., Euskirchen, E., Hugelius, G., Grosse, G., Jones, M., Koven, C., Leshyk, V., Lawrence, D., Loranty, M. M., Mauritz, M., Olefeldt, D., Natali, S., Rodenhizer, H., Salmon, V., Schädel, C., Strauss, J., Treat, C., and Turetsky, M.: Permafrost and Climate Change: Carbon Cycle Feedbacks From the Warming Arctic, Annual Review of Environment and Resources, 47, 343–371, https://doi.org/10.1146/annurev-environ-012220-011847, 2022.

Strom, K. and Keyvani, A.: An Explicit Full-Range Settling Velocity Equation for Mud Flocs, Journal of Sedimentary Research, 81, 921–934, https://doi.org/10.2110/jsr.2011.62, 2011.

Syvitski, J. P. M., Peckham, S. D., Hilberman, R., and Mulder, T.: Predicting the terrestrial flux of sediment to the global ocean: a planetary perspective, Sedimentary Geology, 162, 5–24, https://doi.org/10.1016/S0037-0738(03)00232-X, 2003.

The Great Arctic Rivers Observatory: Water Quality Dataset, Version 20260601, https://arcticgreatrivers.org/data/ (last access: 22 September 2026), 2026.

Thomas, R. G., Smith, D. G., Wood, J. M., Visser, J., Calverley-Range, E. A., and Koster, E. H.: Inclined heterolithic stratification—Terminology, description, interpretation and significance, Sedimentary Geology, 53, 123–179, https://doi.org/10.1016/S0037-0738(87)80006-4, 1987.

Tian, S., Li, D., Zhang, T., McClelland, J. W., Overeem, I., Lane, S. N., Spencer, R. G. M., Wohl, E., Sha, A., Zhao, Y., Miao, C., Ning, M., Yuan, L., and Ni, J.: Increasing river sediment concentration and flux across the pan-Arctic, Nat. Geosci., 19, 565–572, https://doi.org/10.1038/s41561-026-01960-z, 2026.

https://doi.org/10.5194/egusphere-2026-6572
Preprint. Discussion started: 4 November 2026
© Author(s) 2026. CC BY 4.0 License.

Torres, M. A., Limaye, A. B., Ganti, V., Lamb, M. P., West, A. J., and Fischer, W. W.: Model predictions of long-lived storage of organic carbon in river deposits, Earth Surface Dynamics, 5, 711–730, https://doi.org/10.5194/esurf-5-711-2017, 2017.

Tran, D. and Strom, K.: Floc sizes and resuspension rates from fresh deposits: Influences of suspended sediment concentration, turbulence, and deposition time, Estuarine, Coastal and Shelf Science, 229, 106397, https://doi.org/10.1016/j.ecss.2019.106397, 2019.

U.S. Army Corps of Engineers, I. E. G.: CRREL Ice Jam Database, 2026.

Vanoni, V. A.: Transportation of Suspended Sediment by Water, Transactions of the American Society of Civil Engineers, 111, 67–102, https://doi.org/10.1061/TACEAT.0005975, 1946.

Vázquez-Tarrío, D., Piqué, G., Vericat, D., and Batalla, R. j.: The active layer in gravel-bed rivers: An empirical appraisal, Earth Surface Processes and Landforms, 46, 323–343, https://doi.org/10.1002/esp.5027, 2021.

Voepel, H., Schumer, R., and Hassan, M. A.: Sediment residence time distributions: Theory and application from bed elevation measurements, Journal of Geophysical Research: Earth Surface, 118, 2557–2567, https://doi.org/10.1002/jgrf.20151, 2013.

Webster, J. R., Benfield, E. F., Ehrman, T. P., Schaeffer, M. A., Tank, J. L., Hutchens, J. J., and D'Angelo, D. J.: What happens to allochthonous material that falls into streams? A synthesis of new and published information from Coweeta, Freshwater Biology, 41, 687–705, https://doi.org/10.1046/j.1365-2427.1999.00409.x, 1999.

White, K. D.: A New Ice Jam Database, JAWRA Journal of the American Water Resources Association, 32, 341–348, https://doi.org/10.1111/j.1752-1688.1996.tb03456.x, 1996.

Wright, S. and Parker, G.: Modeling downstream fining in sand-bed rivers. I: formulation, Journal of Hydraulic Research, https://doi.org/10.1080/00221680509500381, 2005.

Wysocki, N. and Hajek, E.: Mud in sandy riverbed deposits as a proxy for ancient fine-sediment supply, Geology, 49, 931–935, https://doi.org/10.1130/G48251.1, 2021.

Yoo, K., Mudd, S. M., Sanderman, J., Amundson, R., and Blum, A.: Spatial patterns and controls of soil chemical weathering rates along a transient hillslope, Earth and Planetary Science Letters, 288, 184–193, https://doi.org/10.1016/j.epsl.2009.09.021, 2009.

Yu, B., Dong, H., Jiang, H., Lv, G., Eberl, D., Li, S., and Kim, J.: THE ROLE OF CLAY MINERALS IN THE PRESERVATION OF ORGANIC MATTER IN SEDIMENTS OF QINGHAI LAKE, NW CHINA, Clays and Clay Minerals, 57, 213–226, https://doi.org/10.1346/CCMN.2009.0570208, 2009.

Zeichner, S. S., Nghiem, J., Lamb, M. P., Takashima, N., de Leeuw, J., Ganti, V., and Fischer, W. W.: Early plant organics increased global terrestrial mud deposition through enhanced flocculation, Science, 371, 526–529, https://doi.org/10.1126/science.abd0379, 2021.